Estimation of the Ocean Water Albedo From Remote Sensing and Meteorological Reanalysis Data

Youbin Feng, Qiang Liu, Ying Qu, and Shunlin Liang, *Fellow, IEEE*

***Abstract*—Ocean water albedo (OWA) plays an important role in the global climate variation. Compared with the achievements in land surface albedo studies, the global distributions of ocean water and sea ice albedo are seldom addressed. This study designed an operational global OWA algorithm based on the three-component reflectance model of the ocean water: sun glint, whitecaps, and water-leaving reflectance. The related achievements in these three areas are reviewed and integrated into the operational algorithm. After the sensitive analysis, the algorithm is compared with previous studies and validated with ground observations at COVE site located 25 km east of Virginia Beach (36.91° N, 75.71° W), and the results indicate that the proposed algorithm is generally consistent with previous parameterization scheme. As an example, the global OWAs in summer and winter 2011 are generated using the remote sensing reflectance data sets via the Moderate Resolution Imaging Spectroradiometer and Modern-Era Retrospective analysis for Research and Applications meteorological reanalysis data set. The generated product includes instantaneous (e.g., local noon) and daily mean OWAs under both clear-sky and white-sky conditions. Upon the examples, the local noon clear-sky OWA shows a significant latitude variation due to the dominance of the solar angle, whereas the white-sky OWA is sensitive to wind speeds and optical constituents. The global distribution of the daily mean OWA exhibits a similar trend to the local noon OWA. However, the daily mean clear-sky OWA is significantly larger than the local noon OWA; this finding should be noted when using OWA products for energy balance research. Additionally, all forms of OWA products exhibit increase in coastal areas with high input of terrestrial matters.**

***Index Terms*—Ocean water albedo (OWA), sun glint, water-leaving reflectance, whitecaps.**

Manuscript received May 23, 2014; revised January 8, 2015 and June 22, 2015; accepted July 15, 2015. Date of publication September 2, 2015; date of current version January 19, 2016. This work was supported in part by the International S&T Cooperation Program of China under Grant 2012DFG21710, by the National Natural Science Foundation of China under Grant 41371356 and Grant 41331171, by the National High Technology Research and Development Program of China under Grant 2013AA122801, and by the Project Fund by China Postdoctoral Science Foundation under Grant 2014M550025. *(Corresponding author: Qiang Liu.)*

Y. Feng and Q. Liu are with the State Key Laboratory of Remote Sensing Science, College of Global Change and Earth System Science, Beijing Normal University, Beijing 100875, China (e-mail: robinbird@mail.bnu.edu.cn; toliuqiang@bnu.edu.cn).

Y. Qu was with the State Key Laboratory of Remote Sensing Science, College of Global Change and Earth System Science, Beijing Normal University, Beijing 100875, China. He is now with the School of Geographical Sciences, Northeast Normal University, Changchun 130024, China (e-mail: quy100@nenu.edu.cn).

S. Liang is with the School of Geography, Beijing Normal University, Beijing 100875, China, and also with the Department of Geographical Sciences, University of Maryland, College Park, MD 20742 USA (e-mail: sliang@umd.edu; sliang@bnu.edu.cn).

Color versions of one or more of the figures in this paper are available online at http://ieeexplore.ieee.org.

Digital Object Identifier 10.1109/TGRS.2015.2468054

I. Introduction

COVERING about 70% of the Earth's surface, the ocean serves as the most significant global heat buffer. It absorbs about 95% of incident solar energy in the upper water columns and redistributes heat through large-scale oceanic currents and atmospheric circulation, thus influencing not only the global climate system but also many physical and biological processes of marine ecosystem [1]. The ocean water albedo (OWA), defined as the ratio of the reflected radiation from the ocean water surface to the incident radiation upon it, serves as an indicator of the solar energy distribution and plays an important role in the Earth system.

Nowadays, satellite observations are widely accepted to acquire Earth surface parameters in the global scale. Compared with the numerous land surface albedo products, e.g., MODIS BRDF/albedo product [2], Visible Infrared Imaging Radiometer Suite (VIIRS) albedo product [3], Global Land Surface Satellite (GLASS) albedo product [4], and GLOBALBEDO product [5], however, the OWA product derived from remote sensing is hardly available. For instance, the global albedo product derived from Advanced Very High Resolution Radiometer data set [6], [7] emphasizes more on the sea ice distribution and its impact to ocean surface albedo, whereas the albedo of open water surface is oversimplified. This also leads to the undesirable OWA parameterization in global climate models (GCMs). For instance, after the planetary albedo comparison between satellite measurements [Earth Radiation Budge Experiment and Clouds and the Earth's Radiant Energy System (CERES)] and 20 GCMs by Bender *et al.* [8], near-zero or even negative correlations were found over the ocean. In addition, the poor GCMs' simulation of the effect of solar zenith angle (SZA) to OWA may be responsible for this difference. Another similar study by Wang *et al.* [9] conducted the comparison between satellite-derived albedo from the International Satellite Cloud Climatology Project and simulated surface albedo from 17 GCMs over the northern latitudes of the Western Hemisphere. Apart from the uncertainties in OWA parameters differing from model to model, it also concluded the following: 1) the agreement between GCMs and measurements is dependent on the temporal and spatial variations with aquatic ecosystem conditions, e.g., chlorophyll concentration and suspended particles loading, particularly in coastal waters, and 2) the coarse spatial resolution of GCMs limits the simulation and may bring some errors, particularly, again, around coastal regions. From the above, a physical-based OWA model with high temporal and spatial resolution is needed to simulate global OWA accurately in climate research studies.

On account of the inextricable link between the ocean and the climate, OWA studies originate from climate modeling, but in a simple way. The air–water interface was used to be simplified as a flat surface, and its reflectance was readily determined from Snell's law and the Fresnel reflectance formulae. Combined with later field measurements, the broadband albedo has been presented as a function of the SZA, such as in [10]–[12]. However, the wild ocean is dynamic and seldom calm. Local wind fields force the sea surface to incline and further change the observed reflectance. In response, Hansen *et al.* [13] proposed another formula that considered the impact of wind speed on the basis of Cox and Munk [14], whose pioneering work statistically linked the distribution of declining facets with the near-surface wind speeds. Because the aforementioned parameterizations are just simple fitting formulas and lack physical significance, we will not reprise them in detail. Readers may refer to part 2 of Enomoto [15] for specific expressions.

Physically, the albedo of ocean water depends on the water constituent, sea state, and incoming radiation. It is composed of two radiative components from the air–water interface: reflection from the downwelling radiation in air and refraction from the upwelling radiation in water. Correspondingly, two radiative transfer mechanisms should be clarified to model the OWA: 1) the relationship between the specular reflection of the air–water interface and the wave slope distribution and 2) the process of absorption and scattering that is governed by the optical properties of the water column. The former is modeled in many studies such as those of Duntley [16], Cox and Munk [14], [17], Wu [18], Gordon [19], and Longuet-Higgins [20]; whereas the latter develops into another important branch of oceanography, i.e., ocean color remote sensing, whose history and basic mechanism are illustrated thoroughly in [21]. Due to these efforts, some radiative transfer models of ocean–atmosphere coupling systems emerge, such as Coupled Ocean and Atmosphere Radiative Transfer (COART) [22], MOMO [23], and PCOART [24].

Ideally, these complex radiative transfer models are capable of exploiting OWA information in accordance with different boundary conditions, such as sun-viewing geometries, wind speed, and chlorophyll concentration. However, the implementation of such complex models in an operational system is questionable in terms of the computational cost and efficiency. Some other practical schemes are needed for operational estimation of global OWA.

In [25], the first step is to obtain the spectral water-leaving radiance from remote optical sensors; this upwelling radiance is broken down into two parts: the underwater radiance transmitted through the water–air interface and the radiance due to the Fresnel reflection of sky light off the water surface. Similarly, Koepke [26] regarded the OWA as three components according to different water body reflection types, i.e., foam, glint, and water leaving, and aimed to determine the effective reflectance of oceanic whitecaps over the ocean surface. Sayer *et al.* [27] followed this structure and further modified the weights of these three components to model the sea surface bidirectional reflectance distribution function (BRDF) for along-track scanning radiometers. The COART model developers have recently proposed another similar parameterization through a multiple regression technique over the simulated data from COART [28]. In addition, Mobley and Boss [29] employed EcoLight-S radiative transfer numerical model to approximated global OWA in the visible through the instantaneous and daily mean transmission factor functioned by latitudes, time, winds speeds, and chlorophyll concentrations. The aforementioned designs are characterized by evident physical meaning, simple and straightforward operation, particularly in large-scale research, such as global ocean research. These advantages inform our choice of this scheme. The accuracy of the proposed three-component model relies upon the choice of each component's model, which will be discussed specifically in the next section.

The outline of this paper is as follows. Section II describes the three-component OWA (TCOWA) algorithm in detail and focuses on modifications aimed at operational production; Section III analyzes the sensitivity of OWA with respect to different parameters based on the TCOWA; Section IV evaluates the presented model by comparing it with two other models [28], [30], as well as with measurement data from the NASA CERES Ocean Validation Experiment (COVE) site; then, it presents the generated global OWA product using a preliminary analysis of the difference between the local noon and daily mean OWA under clear-sky and white-sky atmospheric conditions; Section V concludes this paper with a discussion. The primary symbols used in this paper are listed in Table I for clarity.

II. Algorithm Description

Considering both efficiency and accuracy, we choose the TCOWA algorithm to generate the global OWA from remote sensing and meteorological reanalysis data. As shown in Fig. 1, the OWA is modeled as a weighted sum of three components: sun glint, whitecaps, and water-leaving reflectance. Individually, they are as follows.

1) The sun glint reflectance is predicted as a function of the solar-viewing geometries, wind speeds, and directions based on formulations of Cox and Munk [14] and further involves the shadowing factor according to Gordon and Wang [31].
2) The whitecaps are simplified as a Lambertian surface, and their reflectance only exhibits spectral variability in line with Koepke [26].
3) The water-leaving reflectance depends mainly on wavelengths and pigment concentrations [32], while weakly on the solar-viewing geometry and wind field [33].
4) The weight of each component is quantified by whitecap coverage, which is parameterized in terms of the wind speed [34].

When each component is determined, we can obtain the bidirectional reflectance of the ocean water surface. The spectral albedo follows through angular integration. With the narrowband-to-broadband conversion coefficients, the broadband ocean albedo is finally derived.

TABLE I
LIST OF SYMBOLS IN THIS PAPER

Symbol	Description	Unit
	Spectrum / Geometry	
λ	wavelength	nm
Λ	spectral band	nm
θ_s	solar zenith angle	degree
θ_v	view zenith angle	degree
ϕ_s	solar azimuth angle	degree
ϕ_v	view azimuth angle	degree
$\Delta\phi$	relative azimuth angle between solar and view directions	degree
θ'	refracted view zenith angle	degree
ω	the angle between the directions of solar irradiance and facet normal vector	degree
β	the zenith angle of the normal vector of a glint facet	degree
	Ocean surface albedo (OWA) and related quantities	
R_g	bidirectional reflectance of glints	sr^{-1}
R_{ef}	effective reflectance of oceanic whitecaps	dimensionless
R_{wc}	bidirectional reflectance of oceanic whitecaps	sr^{-1}
R_{wl}	bidirectional reflectance of water-leaving	sr^{-1}
R_{rs}	remote sensing reflectance ($\theta_s = \theta_v = 0$)	sr^{-1}
R_{os}	total ocean water surface bidirectional reflectance	sr^{-1}
$\alpha_{bs}(\theta_s, \lambda)$	spectral black-sky albedo	dimensionless
	Ocean surface albedo (OWA) and related quantities	
$\alpha_{ws}(\lambda)$	spectral white-sky albedo	dimensionless
$\alpha_{cs}(\theta_s, \lambda)$	spectral clear-sky albedo	dimensionless
$\alpha(\theta_s, \Lambda)$	broadband albedo	dimensionless
Y	the diffuse light ratio in clear-sky condition	dimensionless
Vr	relative OWA variation	dimensionless
	Aquatic optical properties and derived quantities	
$a(\lambda)$	total absorption coefficient	m^{-1}
$b_b(\lambda)$	backward scattering/ backscattering coefficient	m^{-1}
R_w	irradiance reflectance, defined as the ratio of the upwelling to the downwelling irradiance just beneath the air-ocean interface	dimensionless
$f(\theta_s, Chl)$	the directional factor defined as the ratio of R_w to b_b/a	dimensionless
η_b	the ratio of the molecular backscattering to the total backscattering of water bodies	dimensionless
$Q\begin{pmatrix}\theta_s,\theta',\\ \Delta\phi, Chl\end{pmatrix}$	factor describing the bi-directivity character of $R_w(0^-)$	sr^{-1}
	Air-water interface	
n	refractive index of sea water	dimensionless
$\rho(\omega)$	Fresnel reflectance at the air-sea interface for the scattering angle ω	dimensionless
$r(\theta', \theta_v)$	sea-water interface / internal Fresnel reflectance for the (θ', θ_v) direction	dimensionless
$\bar{\rho}$	mean reflection coefficient for the downwelling irradiance at the sea surface	dimensionless
$\bar{r}$	average reflection for upwelling irradiance at the water-air interface	dimensionless
z'_x, z'_y	components of the normal vector of a glint facet in the wind-direction-based coordinate	dimensionless
ξ, η	normalized form of z'_x, z'_y	dimensionless
σ_x, σ_y	crosswind and upwind root mean square slope of wave facet slopes	dimensionless
P	the probability function for seeing glitter in solar and viewing configurations($\theta_v, \theta_s, \Delta\phi$)	dimensionless
S	shadowing factor, the probability that an individual facet is visible, i.e., not obstructed by another facet	dimensionless
W	whitecaps coverage	dimensionless
	Meteorological parameters	
U_{10}	wind speed at 10m above sea level	m/s
ϕ_w	wind directions	degree

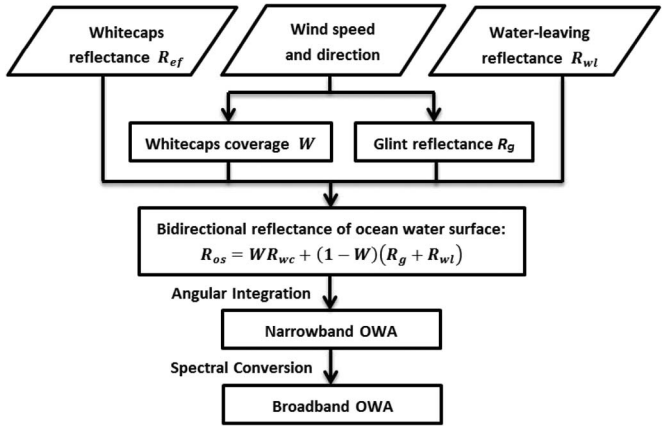

Fig. 1. TCOWA algorithm flowchart.

A. Sun Glint

For an ideally calm water body, the air–water interface becomes a mirror-smooth surface, the sun reflects off the water surface at the same angle ω of the observer. This strong forward reflection over the water surface is called the sun glint. In addition, its reflectance is denoted by the Fresnel reflectance $\rho(\omega)$, which can be precisely calculated through physical law [35].

Natural waters, however, are seldom calm because local wind drives the surface water, resulting in countless tiny wave facets that demonstrate the spatial and temporal variability. When these glints assemble into a certain region known as glitter, the distribution of the facet orientations in this area could be related to the wind field, i.e., the wind speed U and the wind direction σ_w. To account for the skewness and peakedness of these tiny waves, Cox and Munk [14] studied photographs of the glint radiance from aircraft and proposed a probability distribution function of wave slopes. By fitting the measured data with a Gram–Charlier series, the probability distribution function of wave slopes that are able to reflect the sun glint to the aerial observer at a given viewing angle is given by

$$P(z'_x, z'_y) = (2\pi\sigma_x\sigma_y)^{-1}\exp\left(-\frac{\xi^2+\eta^2}{2}\right) \cdot\left\{1-\frac{1}{2}C_{21}(\xi^2-1)-\frac{1}{6}C_{03}(\eta^3-3\eta) +\frac{1}{24}C_{40}(\xi^4-6\xi^2+3)+\frac{1}{4}C_{22}(\xi^2-1)(\eta^2-1) +\frac{1}{24}C_{04}(\eta^4-6\eta^2+3)\right\} \quad (1)$$

where z'_x, z'_y are components of the normal vector of a glint facet in the wind-direction-based coordinate on which the x-axis is directed positively crosswind and the y-axis is upwind; P is the corresponding probability density; σ_x, σ_y are the standard deviation of z'_x, z'_y, respectively; ξ and η are normalized form of z'_x, z'_y as $\xi = z'_x/\sigma_x$ and $\eta = z'_y/\sigma_y$; the skewness coefficients are $C_{21} = 0.01 - 8.6\times10^{-3}U$ and $C_{03} = 0.04 - 0.033U$, and the peakedness coefficients are $C_{40} = 0.40$, $C_{22} = 0.12$, and $C_{04} = 0.23$ (for clean surface). The details of these variables can be found in [14] and [36].

Since the work of Cox and Munk [14], a number of modifications have been proposed from two aspects. First, many

studies have tried to improve the slope statistics based on new measurements. However, Zhang and Wang [37] concluded that the wind-direction-dependent Cox–Munk model has the best performance after a comparison through MODIS measurements with similar models, such as those of Wu [38], Mermelstein *et al.* [39], Shaw and Churnside [40], and Ebuchi and Kizu [41]. Second, it is worth noting that Cox and Munk [14] only took photographs for SZA θ_s less than 35°. The shadowing effect, which means that an individual facet is obstructed by another facet from a certain (usually large) solar/viewing angle, is not considered in their work. This effect would bias the glint albedo as the solar/viewing zenith angle or the sea surface roughness increases. Therefore, a shadowing factor is needed to correct (1). As in [42], the unidirectional shadowing factor $S(\theta_s, \phi_s)$, where ϕ_s is the solar azimuth angle, is formulated as

$$S(\theta_s, \phi_s) = 1/\left(1 + F(v_s)\right) \tag{2}$$

with

$$F(v_s) = \frac{1}{2}\left[\frac{\exp(-v_s^2)}{\sqrt{\pi} v_s} - \mathrm{erf}(v_s)\right]$$
$$v_s = |\cos\theta_s| \Big/ \left(\sigma\sqrt{1 - \cos^2\theta_s}\right)$$

where $\mathrm{erf}(v_s)$ is the error function of v_s, and σ is the square root of the summed square of σ_x and σ_y in (1). Here, we adopt the bidirectional shadowing factor $S(\theta_s, \phi_s; \theta_v, \phi_v)$, where θ_v and σ_v are the view zenith and azimuth angles, respectively, from Gordon and Wang [31], which is proposed as the product of two unidirectional shadowing factors, i.e.,

$$S(\theta_s, \phi_s; \theta_v, \phi_v) = \frac{1}{\left(1 + F(v_s)\right)\left(1 + F(v_v)\right)} \tag{3}$$

and $F(v_s)$ is similarly derived. Therefore, the shadowing-corrected reflectance of the sun glint R_g (sr^{-1}) is then formulated as follows:

$$R_g(\theta_s, \theta_v, \Delta\phi; U, \phi_w) = \frac{\rho(\omega) P\left(z_x', z_y'\right) S(\theta_s, \phi_s; \theta_v, \phi_v)}{4\cos\theta_s \cos\theta_v \cos^4\beta} \tag{4}$$

where β is the zenith angle of the normal vector of a glint facet.

B. Whitecaps

As the wind speed over the ocean surface increases, so does the inclination of wind-generated waves. When waves' bases cannot support their tops, they collapse and "entrain air into seawater forming clouds of bubbles beneath and foamy patches on the sea surface" [43]. This phenomenon is called whitecaps, or foam.

Some studies describe the process from founding to disappearance and distinguish the difference between whitecaps and foam, such as [44]. These descriptions are helpful to give us a clear understanding of this phenomenon, but it is cumbersome to consider all of this complexity in a global OWA algorithm. Therefore, all of the air–water mixtures due to wave breaking refer to whitecaps here.

Because of their varied forms and complex structures, whitecaps are usually simplified as a Lambertian reflector. Related research studies mainly focus on either the spectral property or the whitecap coverage. Start with spectral reflectance. Payne [45] considered whitecaps to be a gray body with a reflectance of approximately 0.5. Afterward, Whitlock *et al.* [46] simulated stable whitecaps in a laboratory by continuously pumping high-pressure air into the water and drew two fundamental conclusions: 1) whitecaps reflectance in visible spectrum are approximately 0.5, but they decrease to 0.46, 0.37, and 0.21 at 1.05, 1.24, and 1. 56 μm, respectively; and 2) the reflectance depends not only on the thickness of whitecaps but also on the composition. On the basis of these indoor data and continuous photographs recording whitecaps at different ages, Koepke [26] proposed an effective reflectance R_{ef} by averaging the whitecaps from fresh/dense ones to decaying ones (see Fig. 2). Therefore, the reflectance in the visible band is smaller (0.22) compared with the study of Whitlock [46]. Some field experiments are then carried out to determine the spectral variation of whitecaps generated by natural waters, such as in [47] over the surf zone and in [48] and [49] over the open sea. All of these field results show a larger decrease in the longer wavelength than Whitlock *et al.* [46]. Apart from these measurements, Kokhanovsky [50] tried to quantify the spectral reflectance of whitecaps in terms of the liquid bulk absorption coefficient and the bubble size and achieved good agreement with the experimental results above. This study attributes the difference to a large quantity of underwater air bubbles, which failed to be simulated in the laboratory.

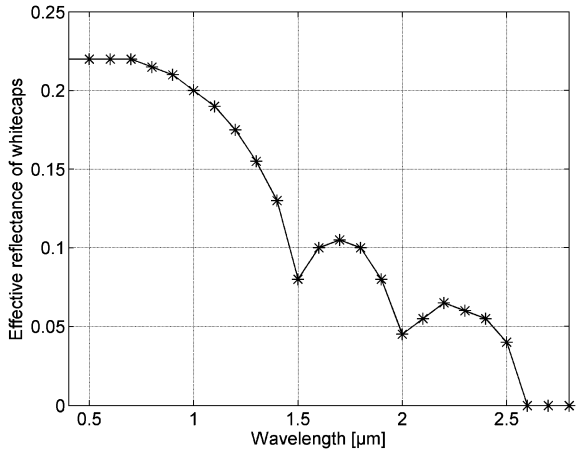

Fig. 2. Effective reflectance R_{ef} (dimensionless) of whitecaps according to Koepke [26].

Based on the preceding discussion, whitecaps over natural waters could never be a simple patch such as a solid block. It is a dynamic or a growing process. The area of an individual whitecap might increase with its age, whereas its reflectance decreases. Therefore, the effective reflectance R_{ef} indicating the average state of whitecaps at different ages is taken into account, and the published data in [26] are adopted in this study.

As shown in Fig. 2, however, this reflectance data cover the spectral range from 0.5 to 2.8 μm, which is narrower than the shortwave range (0.3–5.0 μm) in Section II-E. Considering the spectral stability of whitecaps in the visible, the effective reflectance between 0.3 and 0.5 μm still takes the same value as 0.22. In addition, the reflectance between 2.5 and 2.8 μm

is negligible due to strong absorption of water and takes the value 0 at the longer wavelength in this study.

The whitecap coverage W follows, defined as the fraction of ocean surface covered by whitecaps [51]. The lowest wind speed needed to generate whitecaps is approximately 3 m/s [52]. This is certainly not a universal value because a suite of environmental conditions may also affect the formation of whitecaps, such as the sea surface tension, salinity, current velocity, sea surface temperature, and atmospheric stability denoted by the difference between the seawater and air temperature [48]. Therefore, the whitecap coverage at present is primarily fitted using experimental data in specific environmental conditions and is proposed as a function of wind speed (usually at 10 m above sea level) and atmospheric stability. These equations are reviewed in detail by Anguelova and Webster [43]. Monahan and O'Muircheartaigh [53] had been regarded as the optimal parameterization of W and widely cited [26], [27], [54], however, is now considered more likely to overestimate whitecaps coverage in the open sea [34], and correspondingly lead to an overestimate of ocean water BRDF/albedo and an underestimate of their angular dependence. In this paper, a piecewise wind-speed-only parameterization of W is adopted according to Callaghan *et al.* [34], i.e.,

$$\begin{cases} W = 3.18\times10^{-5}(U_{10}-3.70)^3; & 3.70 < U_{10} \le 10.18 \\ W = 4.82\times10^{-6}(U_{10}+1.98)^3; & 10.18 < U_{10} \le 23.09 \end{cases} \tag{5}$$

where W is a dimensionless value between 0 and 1, and U_{10} is the wind speed at 10 m above sea level (m/s). For U_{10} below 3.7 m/s, we consider there are little whitecaps over the ocean surface and take W as 0. For U_{10} above 23.09 m/s, we still use the second leg of (5).

C. Water Leaving

The water-leaving reflectance $R_{\rm wl}$ is defined as the ratio of the above-surface upwelling radiance exiting the water body to the downwelling irradiance incident on the water surface. This upwelling radiance originates from the absorption and scattering process in waters and the transmission through water–air interface; thus, it varies not only with water constitutes but also with angular geometry. Because the bottom reflectance may significantly modify $R_{\rm wl}$ [55], we only focus on the optically deep water. Following the pioneer work of Gordon [19] and Austin [25] provides widely cited tabulated data of the time-averaged surface reflectance from both the air and water sides. Combined with biooptical models [56], [57], Morel *et al.* [33], [58]–[60] furthered the study of the directional radiance of water bodies and proposed a more complete expression of water-leaving reflectance, i.e.,

$$R_{\rm wl}(\theta_s,\theta_v,\Delta\phi,U,\text{IOP}) = \left\{ \frac{\left(1-\overline{\rho(U)}\right)\left[1-\rho(\theta',\theta_v)\right]}{\left(1-\overline{r(U)}R_w\right)n^2} \right\} \times \frac{f(\theta_s,U,\text{IOP})}{Q(\theta_s,\theta',\Delta\phi,U,\text{IOP})} \times \left(\frac{b_b}{a}\right) \tag{6}$$

where $\Delta\phi$ is the relative azimuth angle between solar and view directions; IOP, short for inherent optical properties, mainly includes the absorption coefficient a and the backscattering coefficient b_b of water bodies; $\overline{\rho(U)}$ and $\overline{r(U)}$ are the mean reflection coefficient for the downwelling and upwelling irradiance at the sea surface, which are functions of wind speed; θ' is the refraction angle; $\rho(\theta',\theta_v)$ is the Fresnel reflectance at the water side at the (θ',θ_v) direction; n is the real part of water refraction index; R_w is the reflectance of water bodies defined as the ratio of the upwelling to the downwelling irradiance just beneath the sea surface, and is usually represented by the product of f and b_b/a [58]; f and Q are the directional factors of water bodies, which are determined by the solar/view geometry, wind speed, and IOP.

The part in curly brace, describing the light propagation through the sea surface, could be referred to studies such as those of Austin [25], Sayer *et al.* [27], and Morel *et al.* [60]. The rest of the variables, namely, a, b_b, f, and Q in natural waters, however, still need to be determined. To estimate the water leaving albedo, TCOWA has two schemes.

The first scheme considers only Case 1 waters. It is assumed that optical properties of Case 1 waters could be adequately predicted from the water column chlorophyll concentration [61]. Therefore, f and Q can be determined by the lookup tables (LUTs) given by Morel *et al.* [33], and b_b and a are estimated according to chlorophyll concentrations as reviewed by Morel and Maritorena [32]. Then, the water-leaving albedo is derived by integration of (6) on solar/viewing geometry.

The Case 1 waters cover about 60% of the global ocean surface [62]. For the rest of the waters, particularly coastal waters around Europe, east coast of Asia, and Irish Sea, their optical properties are hard to be determined due to the complex constitutes generated by biological activities and nonbiological processes (e.g., terrestrial runoff, sediment resuspension by currents, artificial contaminant, or oil spills). Despite recent measurements of a and b_b in certain regions [63]–[66], these results cannot be extended to global usage. Thus, it is necessary to take the advantage of remote sensing data to parameterize the optical properties of natural waters. As the raw remote sensing observations are affected by atmospheric disturbance, solar/view geometry, and sun glints, ocean color researchers usually process the raw data into remote sensing reflectance $R_{\rm rs}$ before further applications. Referring to this specifications [67], it corresponds to the $R_{\rm wl}$ normalized into zenith direction $(\theta_s=\theta_v=0)$, thus providing the most direct information of $R_{\rm wl}$ globally.

The second scheme directly relates the water-leaving albedo with the zenithal $R_{\rm rs}$ through regression technique. To be specific, the $R_{\rm rs}$ product is released by the NASA Ocean Biology Processing Group (http://oceancolor.gsfc.nasa.gov/cms/homepage). We first build a simulated data set of water-leaving spectral reflectance and spectral albedo with (6), considering different chlorophyll concentrations and wind fields, and then employ a quadratic curve-fitting technique to relate the zenithal $R_{\rm rs}$ to the black-sky water-leaving albedo, as shown in Fig. 3. The fitting coefficients, i.e., k_1 and k_2 in Fig. 3, are specific to SZA and wavelength and are stored in an LUT in the operational program. This way, the water-leaving albedo can be calculated from the $R_{\rm rs}$ product. Although the LUT is built for Case 1 waters, it is applied to all kinds of waters, including coastal areas. The accuracy loss is acceptable because (6) only

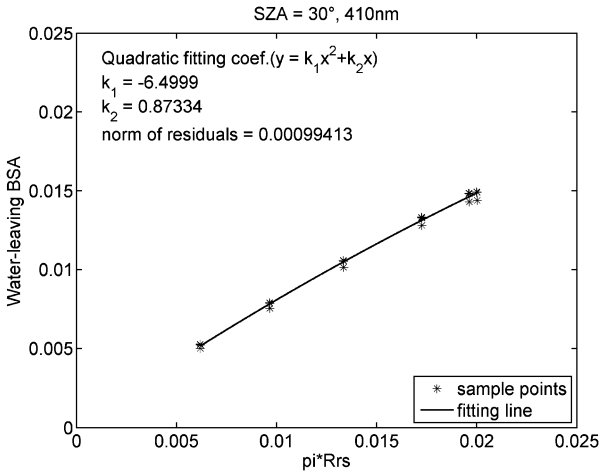

Fig. 3. Example of the conversion coefficients from the zenithal $R_{\rm rs}$ to the water-leaving BSA.

provides the shape of angular variation, which is weak in water-leaving reflectance compared with the spectral variation in the $R_{\rm rs}$ product (see Section III).

D. Spectral OWA

After determining the reflectance of each component, the bidirectional reflectance of the ocean water surface is considered as the weighted sum of the three components, where the weights are functions of whitecap coverage W in terms of wind speed. Koepke [26] started the discussion as follows:

$$R^*_{\rm os} = WR_{\rm ef} + (1-W)R^*_g + (1-WR_{\rm ef})R^*_{\rm wl} \qquad (7)$$

where $R^*_{\rm os}$ is the reflectance of ocean water surface; $WR_{\rm ef}$ is the effective reflectance of the total whitecaps (whatever patches or streaks, newly formed or decayed, multiple layers or single layer) over a certain sea surface; $(1-W)R^*_g$ and $(1-WR_{\rm ef})R^*_{\rm wl}$ are the contributions from the sun glint and water-leaving terms, respectively. All the quantities in (7) are dimensionless in [26]. In order to distinguish them from variables associated with solid angle $(\rm sr^{-1})$ in this paper, they are all labeled $*$ in superscript. To transform a dimensionless variable into its corresponding one associated with solid angle $(\rm sr^{-1})$, it should be divided by π. There are few points to be discussed about (7).

1) The weight of water-leaving $(1-WR_{\rm ef})$. Koepke [26] proposed this weight by assuming that the whitecaps reflectance is on the same order of magnitude as the water-leaving reflectance. It means that the downwelling radiance of the air side could travel through the area covered by whitecaps, then turn into the upwelling radiance owing to the reflection off the water body, and, ultimately, penetrate through the whitecaps and be observed. Sayer *et al.* [27] rewrote the weight of the water-leaving contribution as $(1-W)$ and assumes that the water-leaving radiance could be only observed in a whitecaps-free area, which is the same as the glint radiance. Different from Koepke [26], this assumption implies that whitecaps are opaque mediums that the downwelling radiance in the air or upwelling radiance in water bodies would barely penetrate through. This is reasonable for the following reasons: a) in microcosm, whitecaps consist of a large number of air bubbles that would decrease the downwelling radiation, while increasing the backscattered upwelling radiation [68], and b) in macrocosm, the multiple-layer structure of whitecaps would extend the light beam propagation path and thereby increase the possibility of radiation attenuation due to the water [44].
2) The effective reflectance of whitecaps $R_{\rm ef}$. As shown in Fig. 2, $R_{\rm ef}$ is a measured quantity addressed as bidirectional reflectance factor (dimensionless) in [69]. Because whitecaps are considered as Lambertian reflectors here, we divide $R_{\rm ef}$ by π to denote the BRDF $(\rm sr^{-1})$ of whitecaps, represented by $R_{\rm wc}$.
3) The water-leaving reflectance $R_{\rm wl}$. It is a kind of volume scattering rather than surface reflectance such as those of whitecaps and glints. Due to the nonisotropic structure of the in-water radiative field, the upwelling radiance beneath the ocean surface varies with the solar geometry [70], so as the water-leaving radiance. A disputable point is the difference between the water-leaving reflectance $R_{\rm wl}$ here and the remote sensing reflectance in the literature. $R_{\rm wl}$, formulated by (6), is introduced by Morel *et al.* [33], where the water-leaving radiance is parameterized as solar/view geometry, IOP, and wind speeds (the aerosol optical thickness is also contained but not discussed in this study), and the downwelling irradiance upon the ocean surface depends primarily on the solar geometry. As to the term remote sensing reflectance, four types are usually discussed.
   a) Designed for field measurements, the first one was referred to the ratio of the measured upwelling radiance just above the water surface (consists of the water-leaving radiance and the surface-reflected sky radiance) and the plane downwelling irradiance (integrated by the downwelling radiance in all direction) [71]. Thus, it is a hemispherical-directional quantity.
   b) Differing from the former, the second one employs only the water-leaving radiance as the numerator and the scalar downwelling irradiance (resulting from the plane one divided by the downwelling average cosine) as the denominator, which had been called the remotely sensed reflectance in [72].
   c) The third one is a bidirectional quantity used by Morel and Gentili [60] and Lee *et al.* [73], defined as the ratio of the water-leaving radiance vertically measured and the plane downwelling irradiance. Obviously, the third one coincides with $R_{\rm wl}$ when $\theta_v = 0$.
   d) The last one is applicable to the observation in the space: the water-leaving radiance is further normalized to remove the effect of solar orientation and atmospheric attenuation and then divided by the mean extraterrestrial solar irradiance to generate the product of remote sensing reflectance released by the NASA Ocean Biology Processing Group [67]. Thus, the last one serves as the basic input to the second scheme

of TCOWA to estimate water-leaving reflectance and albedo.

Therefore, the bidirectional reflectance of the ocean water surface $R_{\rm os}$ ($\rm sr^{-1}$) is constructed as

$$R_{\rm os} = WR_{\rm wc} + (1-W)(R_g + R_{\rm wl}). \tag{8}$$

Now, the spectral black-sky albedo (BSA), or directional-hemispherical reflectance, could be derived from integration over the viewing hemisphere of $R_{\rm os}$, and the spectral white-sky albedo (WSA), or bihemispherical reflectance, would result from the integration of the illumination hemisphere of the BSA [69]. The natural albedo is a combination of BSA and WSA and often referred to as blue-sky albedo [69]. However, the common definition of blue-sky albedo does not imply the amount of ambient light, which varies with aerosol loading, cloud status, wavelength, and SZA. For the purpose of defining the daily mean albedo of ocean water surface, a term of clear-sky albedo (CSA) is adopted in this study, in which the amount of ambient light is determined by assuming cloudless sky and small aerosol loading. Thus

$$\alpha_{\rm bs}(\theta_s, \lambda) = 2\int_0^{\pi}\int_0^{\frac{\pi}{2}} R_{\rm os}(\theta_s, \theta_v, \Delta\phi; \lambda)\sin\theta_v\cos\theta_v d\theta_v d\Delta\phi \tag{9a}$$

$$\alpha_{\rm ws}(\lambda) = 2\int_0^{\frac{\pi}{2}} \alpha_{\rm bs}(\theta_s, \lambda)\sin\theta_s\cos\theta_s d\theta_s \tag{9b}$$

$$\alpha_{\rm cs}(\lambda) = Y\alpha_{\rm ws}(\lambda) + (1-Y)\alpha_{\rm bs}(\lambda) \tag{9c}$$

where $\alpha_{\rm bs}$, $\alpha_{\rm ws}$, and $\alpha_{\rm cs}$ denote BSA, WSA, and CSA, respectively; Y is the diffuse light ratio in general clear-sky condition and calculated as $Y = p(\cos\theta_s)^q$, where $p = 0.123$ and $q = -0.8245$ are the empirical coefficients [74].

Obviously, it is time consuming to integrate all of the solar-viewing angles. Considering that the whitecaps are simplified as Lambertian reflectors, its reflectance, BSA, and WSA are the same. We just need to consider the numerical integration of glint and water-leaving reflectance; therefore, two sets of corresponding LUTs are applied to more efficiently generate OWAs on a global scale.

1) LUTs of the BSA and the WSA of glint. Taking the BSA, for example, its dimension is organized as $N(\text{SZA})\times N(\text{wind direction})\times N(U10)\times N(\text{wavelength})$, where $N(\cdot)$ denotes the operator to get the number of values of a variable. Here, the SZA involves 261 values between and including 0° and 0° and 09°, where the first section [0°, 45°] has the interval of 1° linearly, the second section (45°,65°] has the interval of 0.5° linearly, the third section (65°, 80°] has the interval of 0.2° linearly, and the last section (80°, 90°] has the interval of 0.1° linearly; the wind direction is defined clockwise from the north and involves 13 values linearly spaced between and including 0° and 360°; U10 is the wind speed (m/s) measured at 10 m over the ocean surface, with 46 values of which the first section [0, 3] has the interval 0.3 linearly, the second section (3, 6] has the interval 0.5 linearly, and the third section (6, 35] has the interval 1 linearly; the wavelength involves four values, namely, 410, 500, 670, and 850 nm, considering the weak spectral sensitivity of R_g [75].
2) LUTs of the conversion coefficients converting the zenithal remote sensing reflectance $R_{\rm rs}$ to the water-leaving BSA and WSA. These LUTs are the implementation of the second scheme in Section II-C, which consist of regression coefficients as shown in Fig. 3. Still taking the BSA as an example, the dimension is organized as $2\times N(\text{SZA})\times N(\text{wavelength})$. Here, the number 2 denotes the two coefficients of the quadratic curve through the origin; the SZA uses the same setting as that of glint BSA LUT earlier; the wavelength involves 31 values linearly spaced between and including 400 and 700 nm, considering that $R_{\rm wl}$ could be neglected at wavelengths longer than 700 nm due to the spectral absorption of waters.

E. Broadband OWA

The spectral OWA is used to analyze the ocean surface spectrum, whereas the broadband OWA is applicable to estimate the radiation budget. Based on [76], we structure the broadband OWA as the weighted sum of the spectral OWA of different bands, i.e.,

$$\alpha(\theta_s, \Lambda) = \sum_{i=1}^{n} c_i\alpha_i(\theta_s) + c_0 \tag{10}$$

where α represents the broadband OWA, and α_i is the spectral OWA in band i; c_i is the conversion coefficient from the spectral OWA to the broadband OWA, and c_0 is the constant term. Here, the broadband and narrowband OWA data sets use ocean albedo LUTs based on the COART model, which are parameterized as a function of SZA, wind speed, aerosol/cloud optical depth, and chlorophyll concentration [30], and further include the whitecaps contribution according to Koepke [26] and Callaghan *et al.* [34].

Upon the spectral settings, the narrowbands are based on multiband sensors, e.g., MODIS Aqua. In accordance with land surface albedo research studies, three typical broadbands are considered here: the shortwave (300–5000 nm) band, which corresponds to the main wavelength range of incoming solar energy, the visible band (300–700 nm), which characterizes the photosynthetic active radiation, and the near-infrared band (700–5000 nm), which is complementary to the visible band. Through a multivariate linear regression, we could obtain the narrowband-to-broadband OWA conversion coefficient c_i of each band and finally obtain the broadband OWA (see Table II). Following Liang [76], these coefficients are derived for the clear-sky OWA, but can be also applied to the black-sky and white-sky OWAs. Fig. 4 shows the scatterplots of the broadband OWA and the regression results from (10) in different broadbands, as well as for different illumination settings, i.e., clear sky, black sky, and white sky. From Fig. 4, the regression rmses for near-infrared are perceived as larger than that of the visible and shortwave bands. Due to the ocean color research requirement, most of the ocean-observing sensor channels concentrate on the visible wavelength ranges, resulting in the

TABLE II
CONVERSION COEFFICIENTS OF MODIS AQUA OCEAN COLOR BANDS OWA TO BROADBAND OWA

Band number/ spectral range(nm)	SHORTWAVE	Visible	Near-infrared
8/ 405-420	0.0111	0.2163	---
9/ 438-448	0.0786	0.1161	---
10/ 483-493	0.0509	0.2364	---
11/ 526-536	0.1217	0.0848	---
12/ 546-556	0.1654	0.0932	---
13/ 662-672	0.1195	0.1222	---
14/ 673-683	0.1230	0.1235	---
15/ 743-753	0.1570	---	0.8248
16/ 862-877	0.1882	---	0.2550
Constant term	-0.0022	---	-0.0060
RMSE	0.0040	0.0016	0.0057
R^2	0.9914	0.9974	0.9869

reduced accuracy in the near-infrared band. However, because the main factors for deciding the OWA are the distribution of wave slopes and the whitecap coverage, and these two factors are independent from the wavelength, the accuracy of estimating the near-infrared OWA from visible observations is still acceptable. It is also perceivable that there is only a slight increase in the rmses for the black-sky and white-sky OWAs compared with the rmses for the clear-sky OWA, indicating that the coefficients can be applied to all illumination conditions.

III. SENSITIVITY ANALYSIS OF THE TCOWA

As previously discussed, spectral OWA consists of three components, which are determined by common or exclusive variables. For example, sun glint, whitecaps, and water-leaving reflectance are all affected by wind speeds; in contrast, the effect of chlorophyll concentration is limited to water-leaving reflectance in TCOWA. Therefore, this section first analyzes OWA variations with each variable and then illustrates the relative contribution of sun glint, whitecaps, and water-leaving reflectance to OWA.

A. General Sensitivity Analysis of Variables

For a simple estimation of the variation of OWA caused by input variables, the meaningful variation range and typical value are first assigned to each variable (see Table III). The meaningful range is the range of the variable's value as can be encountered in the operational usage of TCOWA in generating the global OWA, excluding those unrealistic singular values such as SZA of 90° or wind speed beyond 35 m/s. Then, the relative OWA variation with respect to a variable is defined as (11), shown at the bottom of the page, where Vr is the relative OWA variation, $f(x)$ represents the calculated CSA by TCOWA model, which is a function of the variable x, x_0 represents a typical value of this variable, and $[x_{\min}, x_{\max}]$ represents the meaningful range of this variable.

The relative OWA variations are also given in Table III. It is perceived that the most sensitive variable in TCOWA is the SZA; then wind speed, wavelength, chlorophyll concentration also play important roles. The influence of wind direction is relatively small compared with others.

B. Characteristics in the Sun Glint OWA

First, we look into the effect of wind speed coupled with wind direction. As wind direction is only considered in the sun glint component, Fig. 5(a) illustrates the variation of sun glint CSA against wind speeds and wind directions at 443 nm. It is apparent that the change of wind speed causes more variation in sun glint CSA than that of wind direction.

Now, combine the influence of SZA. Taking the sun glint CSA under wind direction 120° and wavelength 443 nm as an example, Fig. 5(b) illustrates the variation of sun glint CSA against SZA and wind speeds. When SZA is less than about 65°, the CSA shows small changes from wind speeds 0 to 35 m/s, but when SZA increases, the variation becomes prominent. In addition, the large variation gradient focuses on regions where the sun is near the horizon and the wind speed is small. For examples, the sun glint CSA varies from 0.0860 to 0.0411 in the displayed range of wind speeds when SZA is 65°; however, the variation ranges from 0.2771 to 0.0755 when SZA is 80°; if the wind speed is 1 m/s, the sun glint CSA starts about 0.0258 at SZA of 0°, grows to 0.0849 at SZA of 65°, and then sharply increases to 0.3196 at SZA of 85°.

In addition, the BRDF model of sun glint in TCOWA includes the shadowing factor, as in (3). Compared with the original Cox–Munk model, we think the shadowing factor under increasing wind speeds is needed to be considered based in Fig. 6, of which the relative difference is calculated from the ratio of original to the shadowing-included glint albedo minus 1. For the white-sky glint albedo, the shadowing factor works mainly at larger wind speeds, and the relative difference reaches nearly 30%, which is corresponding to the obstruction of inclining glint facets due to the increasing wind speeds. For the black-sky glint albedo, the shadowing factor works mainly at larger SZA and wind speeds. Taking the wind speed of 20 m/s, for example, the relative difference is about 7% at SZA of 45° and sharply reaches about 38% at SZA of 80°.

C. Characteristics in the Water-Leaving OWA

The water-leaving CSA is functioned by SZA, wind speeds, wavelengths and IOPs. For Case 1 waters, the optical absorption and scattering coefficients could be adequately predicted from the water column chlorophyll concentration. Among these variables, SZA, wind speeds, and wavelengths determine the directivity of light transmittance, whereas the chlorophyll concentration and wavelengths determine the optical properties of

$$Vr = \frac{\max\{f(x)|x \in [x_{\min}, x_{\max}]\} - \min\{f(x)|x \in [x_{\min}, x_{\max}]\}}{f(x_0)} \times 100\% \tag{11}$$

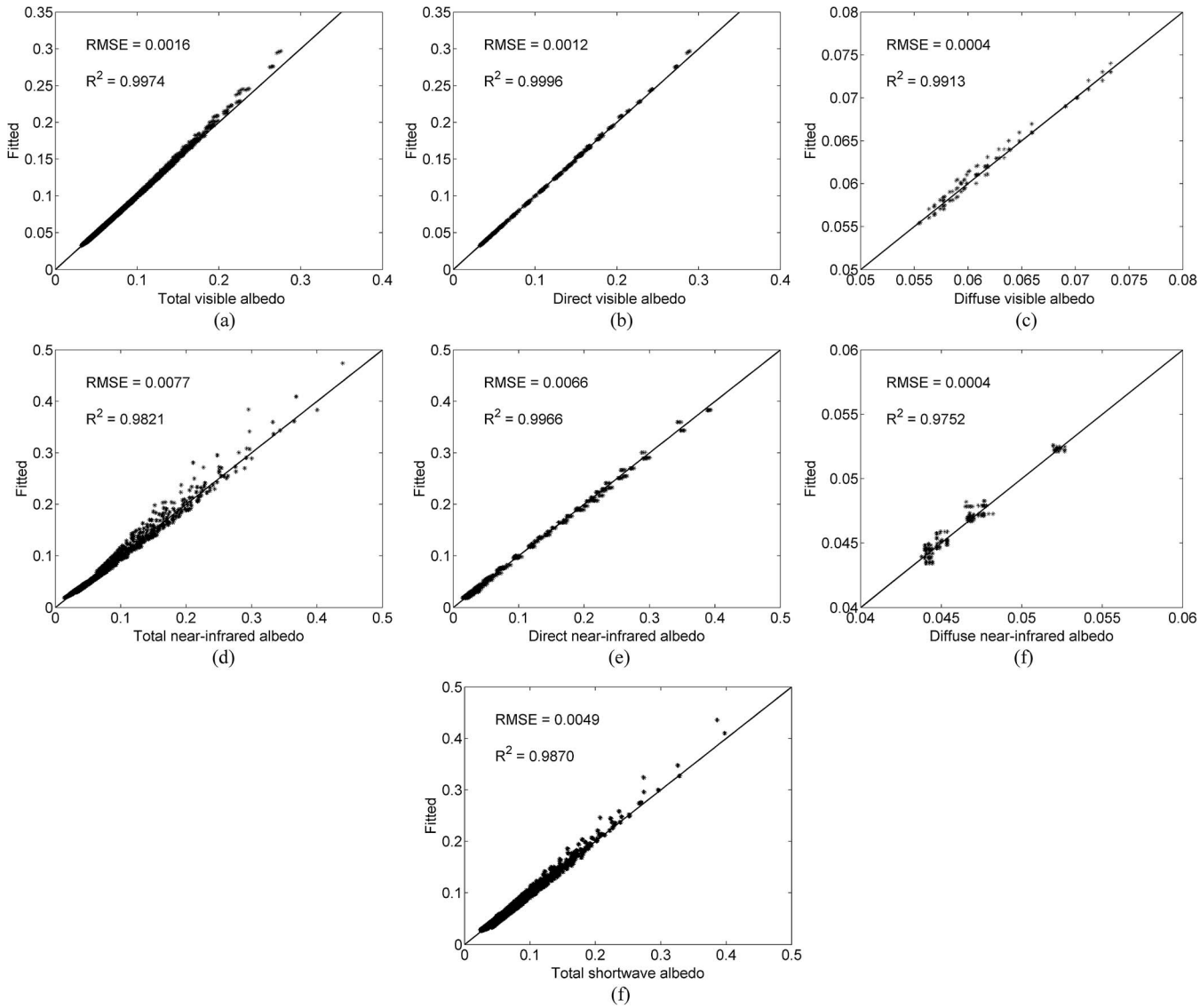

Fig. 4. Simulated visible, near-infrared, and broadband albedos (total, direct, and diffuse) predicted by MODIS Aqua narrowband OWA. (a) CSA in visible band. (b) BSA in visible band. (c) WSA in visible band. (d) CSA in NIR band. (e) BSA in NIR band. (f) WSA in NIR band. (g) CSA in shortwave band.

TABLE III
MEANINGFUL VARIATION RANGE OF VARIABLES IN TCOWA AND THEIR INFLUENCE TO CLEAR-SKY OWA

Variable	UNIT	Meaningful range	Typical value	Relative OWA variation	Influence level
wind speed	m/s	[0, 35]	5	73.70%	Strong
wind direction	(°)	[0, 360]	120	2.63%	Weak
solar zenith	(°)	[0, 85]	45	376.15%	Strong
wavelength	nm	[400, 2500]	443	41.43%	Moderate
chlorophyll concentration	mg/m^3	[0, 12]	0.5	25.13%	Moderate

water bodies. From Fig. 7(a), where SZA is 45° and chlorophyll concentration is 0.5 mg/m^3, the spectral water-leaving CSA shows small changes in the displayed range of wind speeds. From Fig. 7(b), where SZA is 45° and the wind speed is 5.0 m/s, the spectral water-leaving CSA shows obvious changes against the displayed chlorophyll concentration. The water-leaving CSA decreases with chlorophyll concentration at shorter wavelengths, e.g., 412 and 448 nm, and increases at longer wavelengths, e.g., 551 and 678 nm. The maximum absolute variation appears at 412 nm, whereas the maximum relative variation is at 678 nm, as the absolute water-leaving signal is low. From Fig. 7(c), where chlorophyll concentration is 0.5 mg/m^3 and the wind speed is 5 m/s, the variation of water-leaving CSA shows less angular dependence compared with those of sun glint CSA. However, the variation along wavelengths is more obvious than those of sun glint BSA. For an example, it varies from 0.0150 at 412 nm to 0.0008 at 678 nm, when SZA is 45°.

D. Contribution of the Three Components in OWA

Apart from the sun glint and water-leaving component, the influence of whitecaps could not be overlooked in the global scale. The whitecaps here are approximated as Lambertian reflectors, their albedo only varies with wavelengths as shown in Fig. 2. For a calm ocean surface, the contribution of whitecaps

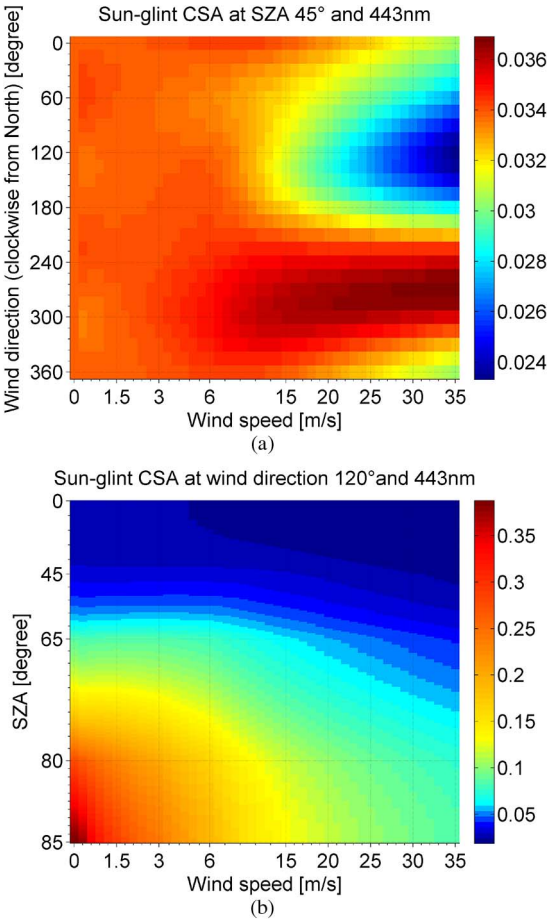

Fig. 5. Variations of sun glint albedo at 443 nm. (a) Sun glint CSA (SZA 45°) against wind speeds and wind directions. (b) Sun glint CSA (wind direction 120°) against wind speeds and SZA. Note that the axes of wind speeds and SZA are distributed in accordance with those of glint albedo LUTs in Section II-D.

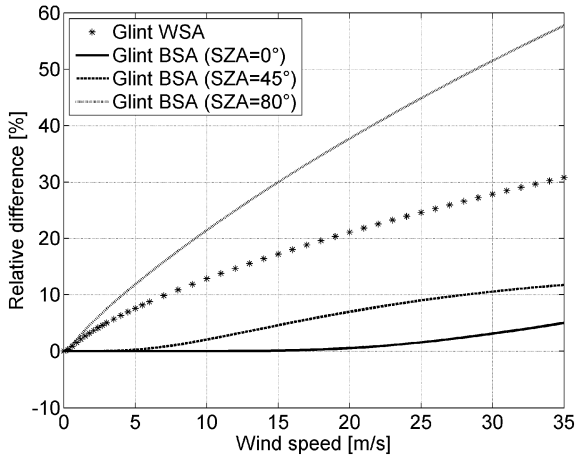

Fig. 6. Relative difference between the original and shadowing-included glint albedo, where the wind direction is 120° and the chlorophyll concentration is 0.5 mg/m^3.

to the OWA is relatively small, as illustrated in Fig. 8. The ocean water BSA in large SZAs generally decreases with wind speed due to the effect of shadowing. As the integration of BSA, the WSA mildly decreases with wind speed when it is less than 30 m/s. However, it is regulated by whitecap coverage and starts to increase when wind speed exceeds 30 m/s.

In order to illustrate the relative contribution of sun glint, whitecaps, and water leaving to the OWA in different conditions, the ternary plots, which use a triangle to display the proportions of three components that sum to a constant, are adopted here. For a given point in a ternary plot, the fraction of each component is determined by first identifying the original point (labeled 0 in the plot) of the component's axis, then identifying the adjacent axis also through the original point, and, finally, drawing a line parallel to the adjacent axis and through the point to be read. The value of the intersection point in the component's axis is the fraction of the component ranging from 0% to 100%.

Fig. 9 presents the ternary plots of the white-sky OWA at three typical wavelengths. At 443 nm [see Fig. 9(a)], the sun glint dominates the OWA at usual wind speeds (0–25 m/s). Taking the light green dot (wind speed of 10 m/s and chlorophyll concentration of 0 mg/m^3), for example, the contributions of sun glint, water leaving, and whitecaps are 0.0489, 0.0166, 0.0017, respectively, and thus introduce the percentages of 72.76%, 24.70%, and 2.54%. As wind speed increases, the contribution of whitecaps increases, whereas those of sun glint and water leaving decrease due to the multiple scattering of the rugged sea surface. Taking the silver gray dot (wind speed of 35 m/s and chlorophyll concentration of 0 mg/m^3), for example, the contributions of sun glint, water leaving, and whitecaps are 0.0236, 0.0134, 0.0536, respectively, and introduces the percentages of 26.05%, 14.79%, and 59.16%.

Now, pay attention to the chlorophyll concentration as indicated by the shape of markers in the figures. Taking the light green markers (wind speed of 10 m/s) at 443 nm, for example, the water-leaving contribution decreases to 9.37%, when the chlorophyll concentration increases to 12 mg/m^3. This is due to the strong absorption of phytoplankton at blue band. For the WSA at 551 nm, however, the water-leaving proportion increases from 4.59% at nil chlorophyll concentration to 16.09% at chlorophyll concentration of 12 mg/m^3 because of strong reflection of phytoplankton at green band. For the red band (667 nm), the water-leaving contribution varies in the same trend like those at blue band (443 nm), but the overall proportion of water leaving declines obviously compared with those of shorter wavelengths due to the strong absorption of water bodies at red band.

Further consider the clear-sky OWA, which is governed by SZA and wind speeds. Fig. 10 is presented at 443 nm and chlorophyll concentration of 0.5 mg/m^3. Like the white-sky OWA, the sun glint accounts for the highest proportion of the clear-sky OWA at usual wind speeds. Taking the light green dot (wind speed of 10 m/s and SZA of 0°), for example, the contributions of sun glint, water leaving, and whitecaps are 0.0235, 0.0121, 0.0017, respectively, and thus introduce the percentages of 63%, 32.44%, and 4.56%. As wind speeds increases, sun glint and whitecaps contribute to the clear-sky OWA in the same way as the white-sky OWA, and their proportions change to 18.65% and 68.65%, respectively, when the wind speed increases to 35 m/s and the sun stays in zenith direction, as shown by the silver gray dot.

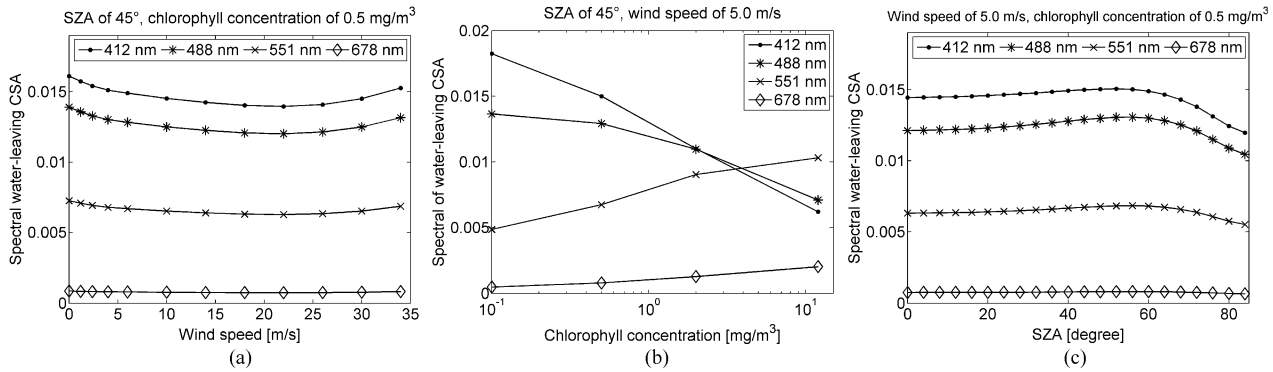

Fig. 7. Variations of spectral water-leaving albedo. (a) Water-leaving CSA against wind speeds when chlorophyll concentration is 0.5 mg/m^3. (b) Water-leaving CSA against chlorophyll concentrations when the wind speed is 5 m/s. (c) Water-leaving CSA against SZA when the chlorophyll concentration is 0.5 mg/m^3 and the wind speed is 5 m/s.

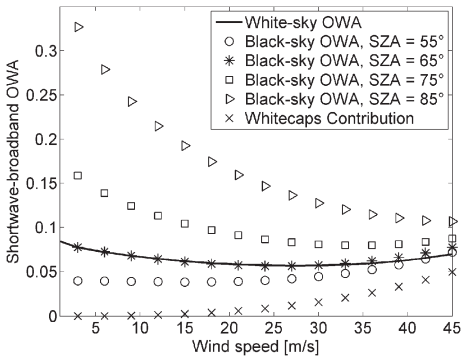

Fig. 8. Shortwave broadband OWA variations against wind speeds (wind direction of 120°).

However, the whitecaps gradually lost the superiority along with the increase of SZA, although the sea surface is still windy. This happens because of the sharp increase of sun glint BSA at large SZA. First, take the cross markers (SZA of 30°) as examples, the whitecaps proportion increases from 0% to 68.16% and the sun glint proportion decreases from 66.65% to 18.95% when the wind speed ranges from nil to 35 m/s. As for the pentagram markers (SZA of 75°), the whitecaps proportion increases from 0% to 48.72%, and the sun glint proportion decreases from 93.67% to 42.57%.

IV. Evaluation and Results

To evaluate the three-component OWA model, we first compare the ocean water BSA and WSA with the parameterizations from Jin *et al.* [28], considering the direct and diffuse incident radiance separately; then, we validate the clear-sky OWA using two data sets: 1) the measurement data from the marine platform COVE, which provide the community with routine measurements of upwelling and downwelling radiation at the sea surface (URL: http://cove.larc.nasa.gov/), and 2) the simulated data set from the COART model, which is also validated by COVE measurements [30]. After that, some global OWA examples of TCOWA estimation are presented and analyzed in terms of their spatial and temporal variations.

A. Comparison of Spectral OWA

Considering the most sensitive OWA parameters (e.g., SZA, wind speeds, aerosol optical depths, and oceanic optical properties), Jin *et al.* [28] divided the OWA into the direct and diffuse components and then separated each component into contributions from the surface reflection and the water body scattering. The four components are independent of each other and depend on different parameters. Therefore, this parameterization (represented by JZ11 in the following) is readily compared with the TCOWA-derived ocean water surface BSA and WSA.

The isotropic Cox–Munk model is employed to parameterize the surface reflection in JZ11, whereas the anisotropic one (1) is employed in our studies; therefore, the contribution of the wind direction to the glint albedo is displayed first. Fig. 11 shows that the influence of wind direction could be neglected if the SZA is less than approximately 50°; however, the wind direction contribution becomes noticeable at large SZA as the wind speed increases. On behalf of inspecting the instantaneous OWA on a global scale, we adopt the anisotropic Cox–Munk model for glint albedo computation. Meanwhile, because the discrepancy between the anisotropic glint BSA and the isotropic one is minimal when the wind direction is around 60°, our results are confined to this angle in the following comparison with JZ11. Fig. 12 presents the ocean surface spectral BSA comparison between JZ11 and TCOWA at different wind speeds and wavelengths.

According to Fig. 12, the shapes of the spectral BSA from JZ11 and TCOWA are similar: each BSA curve is almost constant when the SZA is below approximately 40° and increases sharply after this angle. With respect to spectral variations, the BSA decreases with an increase in the wavelengths due to water absorption. However, discrepancies of the spectral BSA from these two models become significant as wind speed increases. Because JZ11 and TCOWA include the same parameterization of whitecaps reflectance, the reasons leading to the difference may lie in glint/surface direct reflection and water-leaving/water direct scattering. Figs. 13 and 14 present a detailed comparison of these two aspects.

The discrepancies, averaged at all three wind speed levels, between the surface direct reflection in JZ11 and the glint in

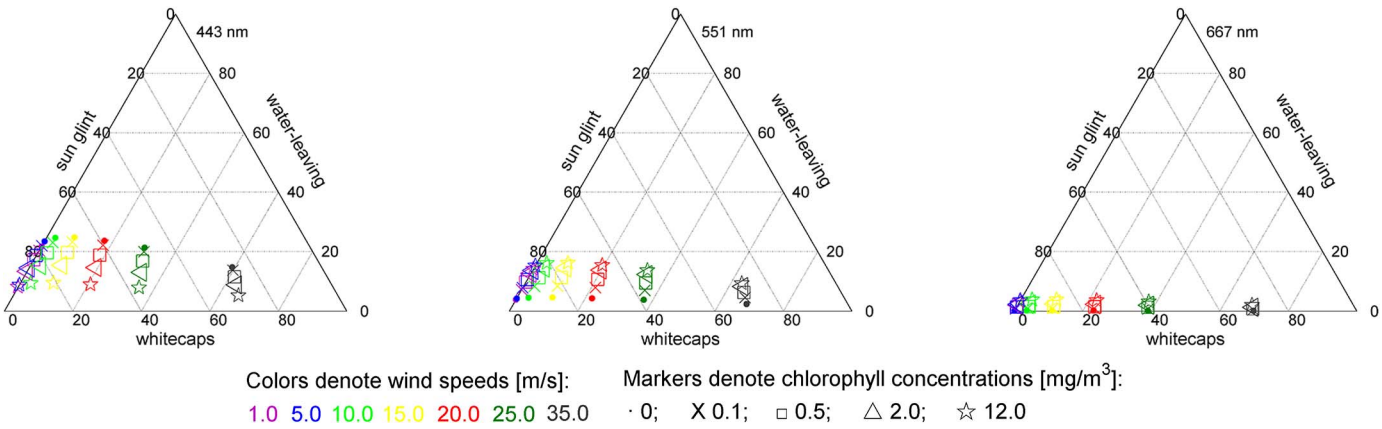

Fig. 9. Relative contributions of sun glint, whitecaps, and water leaving to spectral white-sky OWA. Wind speeds and chlorophyll concentrations are respectively denoted by different colors and markers, as shown in the legend.

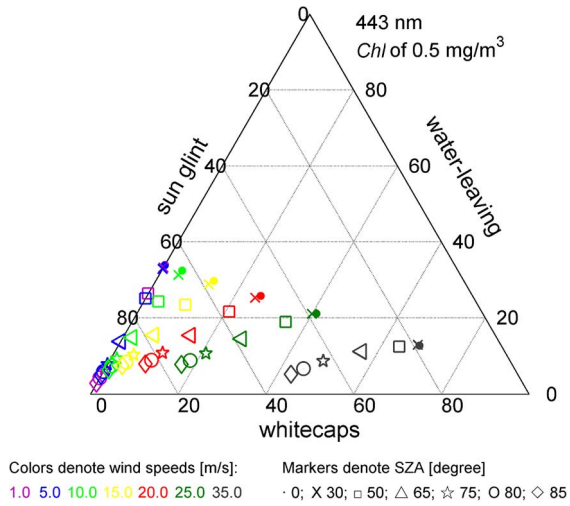

Fig. 10. Relative contributions of sun glint, whitecaps, and water leaving to spectral clear-sky OWA. *Chl* in the figure is short for chlorophyll concentration. Wind speeds and SZA are relatively denoted by different colors and markers, as shown in the legend.

TCOWA are 0.0061, 0.0163, and 0.0392 at SZAs 60°, 70°, and 80°, respectively (see Fig. 13). In addition, the discrepancies between the direct water scattering from JZ11 and the water-leaving BSA from TCOWA are 0.0027, 0.0032, and 0.0035, respectively (see Fig. 14). It is obvious that the specular reflectance over the ocean surface is the primary reason for this difference. More specifically, the differences are as follows: 1) JZ11 considers the shadowing effect according to Sancer [77], whereas TCOWA is based on Gordon and Wang [31], which results in differences when SZA $>$ 80°; 2) JZ11 introduces the multiple scatterings among wind-rippled facets [22], whereas TCOWA only considers the single scattering reflectance for computational simplicity, which explains the differences when 70° $<$ SZA $<$ 80°; and 3) JZ11 adopts Gaussian numerical integration, whereas TCOWA adopts trapezoidal integration in (9), which also incorporates some differences, particularly for large SZA.

It should be also noted that the water-leaving BSA in JZ11 shows more significant directivity than TCOWA in Fig. 14. In addition to the directional influence from the air–water interface, the scattering of water bodies may also raise this directional difference. JZ11 is parameterized from the COART model [22], where the f factor in (6) is based on the expression from Morel and Gentili [58], i.e.,

$$f(\theta_s, \eta_b) = (0.6279 - 02227\eta_b - 0.05113\eta_b^2) + (-0.3119 + 0.2465\eta_b)\cos\theta_s \quad (12)$$

where η_b is the ratio of the molecular backscattering to the total backscattering of water bodies. In TCOWA, f is based on the results given by Morel *et al.* [33] considering Raman scattering. Since both parameterizations are proposed by the same research group, it might be reasonable to assume that the recent one is preferable. Nevertheless, discrepancies in the irradiance reflectance of water bodies are insignificant at an order of 10^{-3}.

B. Validation of Broadband OWA

The preceding section demonstrates that TCOWA is consistent with existing mature models, whereas this section focuses on its validation against field measurements from the COVE site, which is 25 km east of Virginia Beach in the Atlantic Ocean. Because it is near the mouth of Chesapeake Bay, all the radiation measurements are taken over the Case 2 water of which the suspended particles are not only from phytoplankton but also from mineral particles transported by terrestrial runoff. The following validation proves the advantage of TCOWA employing $R_{\rm rs}$ to quantify the water-leaving reflectance of natural waters rather than the biooptical models, which is only applicable to Case 1 waters. Although the optical property of a single site could not confirm a global-scale model adequately, this section is still valuable because COVE is the only available site providing continuous and qualified radiation measurements above ocean surface as far as we know.

All the measurements used are qualified by the Baseline Surface Radiation Network. Specifically, the upwelling broadband solar irradiances are observed by a Epply PSP pyranometer from 0.28 to 4.0 μm; the downwelling broadband irradiances, including direct and diffuse components, are measured by a Kipp&Zonen CH1 pyranometer and a Shaded Kipp&Zonen CH31 pyranometer from 0.2 to 4.0 μm, respectively [78]. The spectral difference between measurements and the modeled

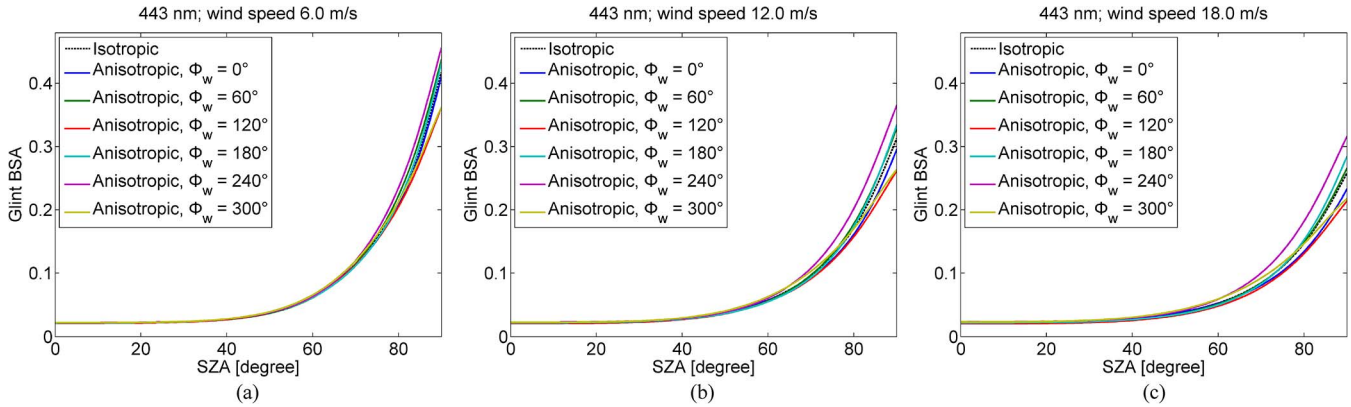

Fig. 11. Comparison of glint BSA (443 nm) as functions of SZAs under different wind directions ϕ_w. (a) Wind speed of 6 m/s. (b) Wind speed of 12 m/s. (c) Wind speed of 18 m/s.

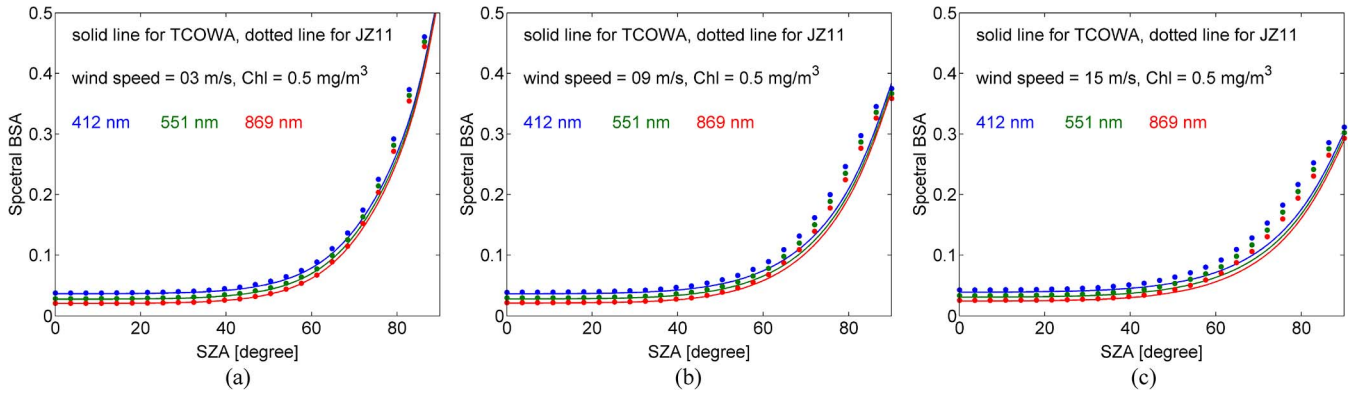

Fig. 12. Ocean surface spectral BSA comparison between JZ11 and TCOWA at different wind speeds. Chlorophyll concentrations are all set to be 0.5 mg/m^3. (a) Wind speeds of 3 m/s. (b) Wind speeds of 9 m/s. (c) Wind speeds of 15 m/s.

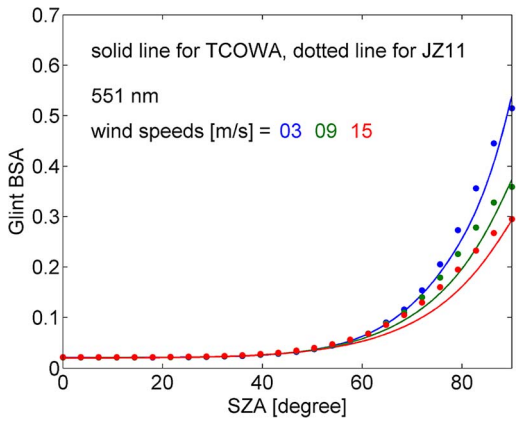

Fig. 13. Comparison between direct surface reflection from JZ11 and glint BSA from TCOWA.

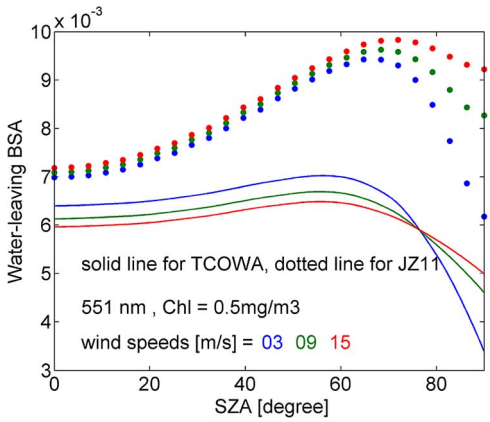

Fig. 14. Comparison between direct water scattering from JZ11 and water-leaving BSA from TCOWA.

shortwave OWA $(0.3-5.0\ \mu\text{m})$ is negligible due to the minor incident solar radiation outside the range of $0.3-3.0\ \mu$m.

As it is almost impossible to validate a BSA and a WSA that represent extreme cases under completely direct and diffuse illumination [79], we first combine the BSA and the WSA into the CSA with the factor of diffuse light ratio [74]. Next, a group of measured CSA of various solar angles and atmospheric conditions are chosen as validation data, and the model predictions are obtained with the corresponding wind speeds and wind directions. Recalling that the water-leaving contribution could either be estimated from chlorophyll concentrations based on (6) or from the zenithal R_{rs} based on conversion coefficients from the last paragraph in Section II-C; TCOWA would generate two sets of broadband OWA to demonstrate the impact of different input schemes. The chlorophyll concentration and R_{rs} around the COVE site are taken from MODIS Aqua Level-3 products provided by the NASA Ocean Biology Processing Group (displayed results refer to http://oceancolor.gsfc.nasa.gov/cgi/l3).

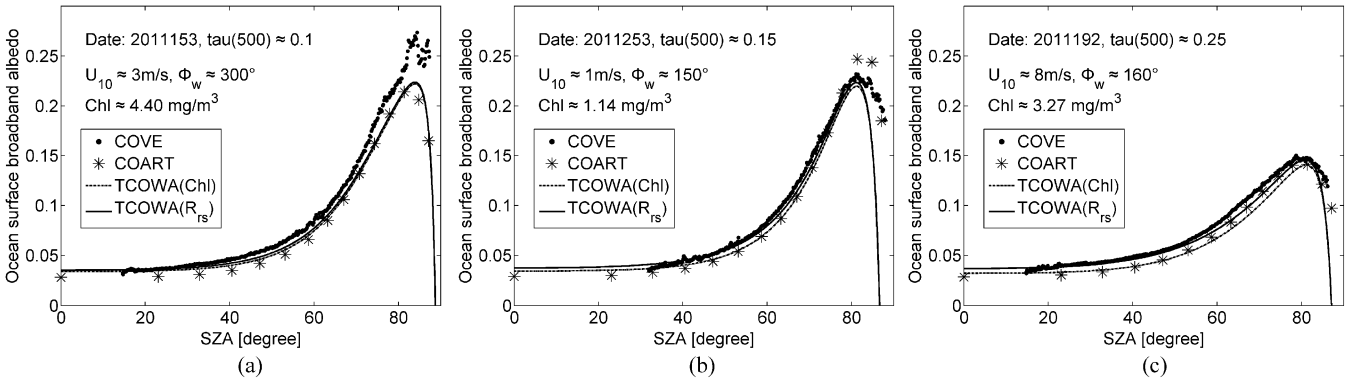

Fig. 15. Validation of the broadband OWA from TCOWA. (a)–(c) COVE measurements of different atmospheric, wind field, and chlorophyll concentrations in three days, whereas model predictions are obtained with corresponding conditions indicated in figures.

As shown in Fig. 15, TCOWA is consistent with the COVE measurements and the COART LUT (supplemented with the whitecaps contribution) in the whole incident hemisphere. They are all nearly constant in the small SZA and grow rapidly thereafter, which is attributed to the strong forward glint scattering. As the sun approaches the horizon, the path of downwelling irradiance becomes the largest, so does the proportion of diffuse irradiance. This explains OWA's sudden drop when the SZA comes close to 90°. The atmosphere optical thicknesses at 500 nm are about 0.1, 0.15, and 0.25 in Fig. 15(a)–(c), respectively. The high optical thickness could decrease the OWA in a large SZA.

Another point is the difference induced by different input schemes. Since the light scattering from suspended mineral particles dominates the water-leaving signal of coastal waters [65], the water-leaving contribution would be underrated if we still apply the biooptical scattering model. Likewise, Jin *et al.* [78] concluded that scattering by coastal sediments could increase the broadband OWA by 0.01 through measurements from Gould Jr. *et al.* [80]. In Fig. 15, the particulate inorganic carbon concentrations $(\mathrm{mol/m^3})$ from MODIS Aqua around the COVE site are 0.0000, 0.0015, and 0.0018 for the three days, respectively. The input scheme, which used R_{rs} (solid line) instead of the concentration of optical constituents (dotted line), makes up the discrepancies [the absolute error by approximately 0.01 and the relative error by approximately 16.7% in Fig. 15(c)] between the biooptical model and the actual situation.

C. Global OWA Estimation

TCOWA is designed to estimate the OWA upon the global scale. As an example, instantaneous (e.g., local noon) and daily mean global OWAs in 9-km spatial resolution and one-day interval are generated with remote sensing and meteorological reanalysis data in the winter and summer of 2011. Specifically, the remote sensing reflectance data from MODIS Aqua Level-3 seasonal products provided by the NASA Ocean Biology Processing Group are used to obtain the water-leaving contribution; the hourly eastward and northward wind speeds at 10 m above the sea surface from the Modern-Era Retrospective analysis for Research and Applications (MERRA) reanalysis data set, which is included in data field shortened as *MAT1NXSLV* in the vast MERRA system (http://gmao.gsfc.nasa.gov/research/merra/file_specifications.php), are used to estimate the glint albedo and whitecaps coverage; the spectral reflectance of whitecaps is in line with Koepke [26].

1) Clear-Sky and White-Sky Local Noon OWAs: In consideration of user's convenience, the global OWA algorithm does not simulate various aerosol optical depths at present, but generates global OWA under two common atmospheric conditions: the clear sky and the white sky. Here, the CSA is generated instead of the traditionally used BSA because the BSA becomes unrealistically large at large SZAs and cannot reflect the state of the actual albedo, whereas the CSA is the actual albedo under cloud-free and low-aerosol loading conditions.

Fig. 16(a) and (b), present the global clear-sky OWA at local noon on February 3 and August 3, 2011, respectively. The wind speed and direction corresponding to the local noontime are extracted from the hourly values of the MERRA data set. Fig. 16 shows a significant seasonal variation of the global clear-sky OWA and clear dependence on latitudes. The clear-sky OWA is relatively small at low latitudes where the sun is high and grows along the northern and southern sides. The Northern Hemisphere is in winter on February 3, and the sun is low even at local noon. This results in a larger clear-sky OWA in the Northern Hemisphere than in the Southern Hemisphere on February 3. It is the other way around on August 3. Therefore, the solar angle is the dominant determinant of the clear-sky OWA at local noon.

Fig. 17 presents the global white-sky OWA at the same time as in Fig. 16. In contrast to the clear-sky OWA, the white-sky OWA does not relate to the solar angle and thus shows no dependence on latitude. The main determinant of the white-sky OWA variation is the wind field and optical constituents. Fig. 18 gives the global wind speed extracted from the MERRA data set on the corresponding time. It is clear that the white-sky OWA has a similar variation pattern to the wind speed in most areas. However, in coastal waters with high optical constituent levels, such as the Black Sea and the east coast of Asia, the contribution of water-leaving reflectance is evident and gives rise to a regional OWA. This can be also observed in the clear-sky OWA (see Fig. 16).

It is also interesting to note that areas with higher wind speeds show lower white-sky OWA in Fig. 17, for instance, in the northern Atlantic Ocean or the southern Pacific Ocean. This

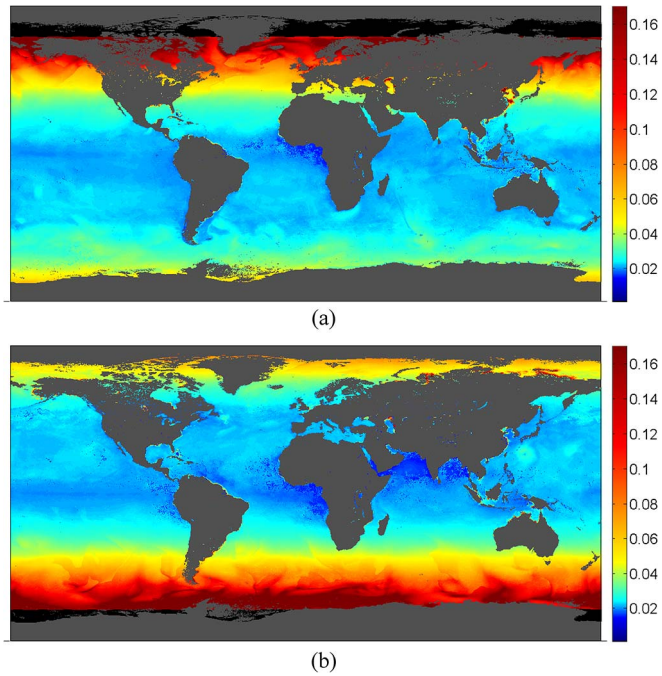

Fig. 16. Clear-sky local noon global OWA on (a) February 3 and (b) August 3, 2011. SZA more than 88° is voided and marked in black.

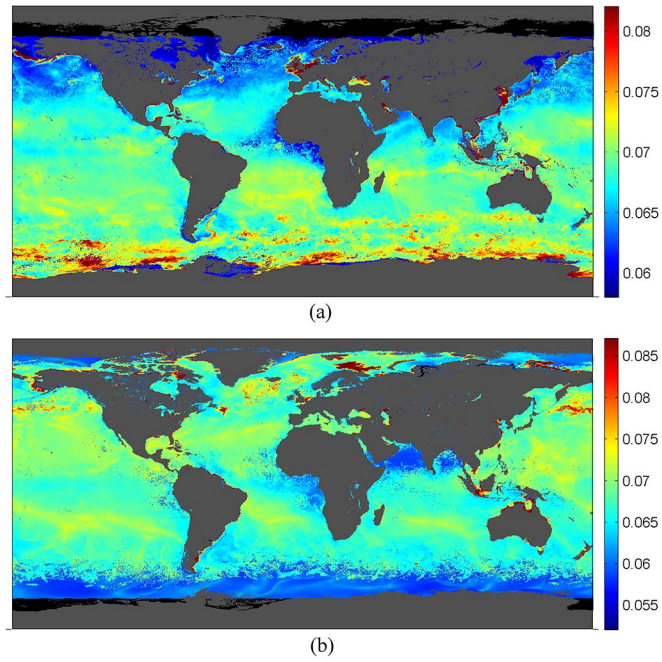

Fig. 17. White-sky local noon global OWA on (a) February 3 and (b) August 3, 2011. SZA more than 88° is voided and marked in black.

is the integrated result from the glint and whitecap coverage, which are both primarily driven by wind. As illustrated in Fig. 8, the contribution of whitecaps to the OWA is small in normal wind speed (less than 30 m/s); thus, the ocean water WSA mildly decreases with wind speed as the result of shadowing the sun glint.

2) Daily Mean and Local Noon OWAs: Unlike the land surface albedo, whose diurnal variation is small compared with the local noon albedo, the clear-sky OWA can change from less than 0.05 to more than 0.2 during a single day [e.g., Fig. 15(a)]. With this consideration, the daily mean clear-sky OWA and white-sky OWA are derived from the TCOWA model, along with the local noon OWA. The daily mean OWA is defined as the energy-weighted average of all instantaneous OWA [81]. Accordingly, the daily mean clear-sky OWA and the white-sky OWA are averaged on their hourly counterparts weighted by the cosine of SZA, and thus integrate the effects from the SZA and wind speeds throughout the day.

Fig. 19(a) and (b) present the global daily mean clear-sky OWA and white-sky OWA on February 3, 2011, respectively. For the white-sky case, the daily mean and local noon OWAs exhibit nearly the same pattern because their driving factor, i.e., the wind field on the global scale, exhibits slight change during one day. For the clear-sky case, the daily mean OWA also reveals its dependence on latitude and season, just like the local noon OWA. However, its value is generally larger. From Fig. 20, which illustrates the zonal averages of OWA, we easily find that these two cases had slight difference in the high latitudes of the Northern Hemisphere and stable difference between 0.02 and 0.04 toward the south. This finding is basically caused by the sharp increase of the glint BSA approaching sunrise and sunset. In February, the sun is usually low around the Arctic, and thus explains the small difference between the

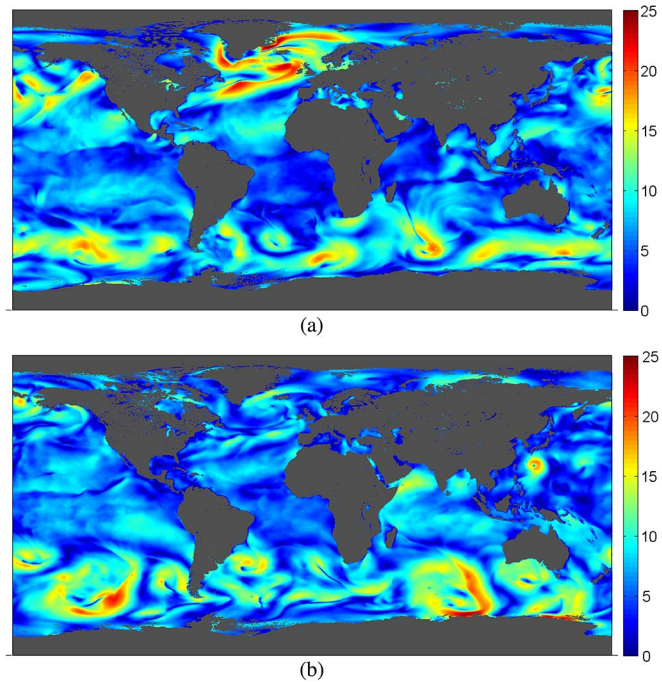

Fig. 18. Local noon global wind speeds (m/s) on (a) February 3 and (b) August 3, 2011.

instantaneous and daily mean cases. For the rest of the latitudes, however, the local SZA is the smallest at noon, and usually brings the smallest clear-sky OWA during the day. Therefore, the daily mean clear-sky OWA can be significantly larger than the local noon clear-sky OWA. As for the coastal areas, the daily mean OWA is also influenced by the high input of terrestrial matter.

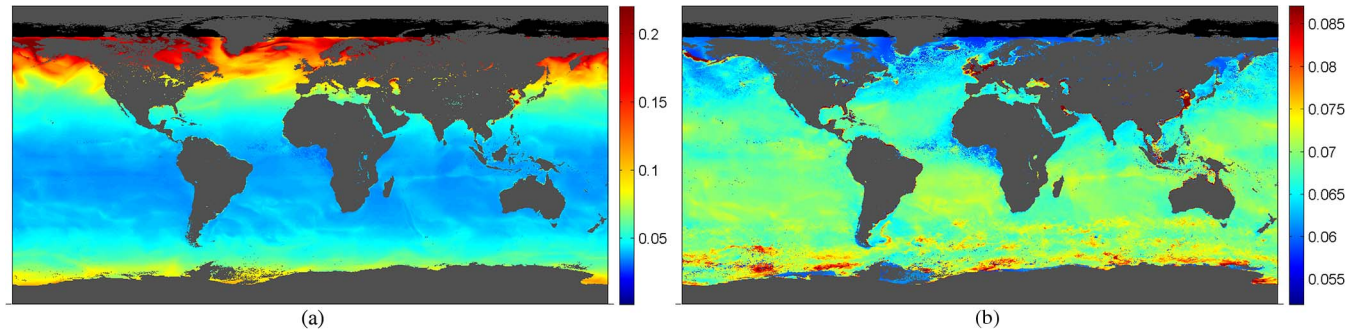

Fig. 19. Global daily mean (a) clear-sky and (b) white-sky OWA on February 3, 2011. SZA more than 88° is voided and marked in black.

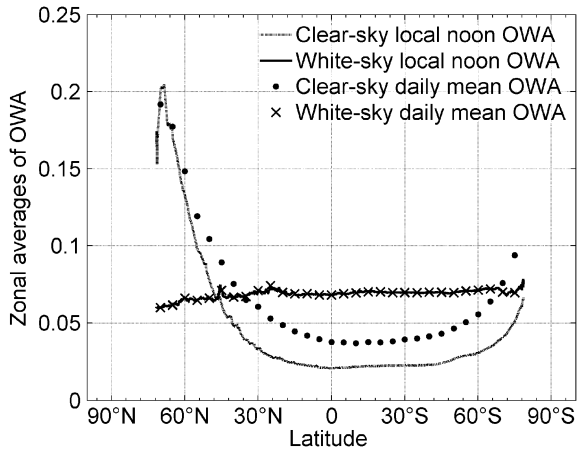

Fig. 20. Zonal averages of OWA in different latitudes on February 3, 2011.

V. Discussion and Conclusion

The OWA is an important factor in the global energy budget. However, research about OWA is relatively scarce compared with the land surface albedo research, and a high-quality global OWA product is greatly needed. In order to provide a more realistic description of the spatial and temporal variation of albedo of the vast ocean than the simple parameterization schemes in most current climate models, the three-component model of OWA (TCOWA) is proposed as an extension to the algorithm of new version of GLASS albedo product to operationally generate the global OWA product from remote sensing and meteorological reanalysis data.

The TCOWA algorithm is characterized by its efficiency without loss of accuracy. All of the three contributors to the OWA, i.e., glint, whitecaps, and water leaving, are flexibly modeled and improved according to the latest developments in corresponding areas. Here, we model the glint reflectance based on the work of Cox and Munk [14] and further consider the shadowing between wind-titled waves. The whitecaps are currently assumed to be Lambertian reflectors because their formation process and light-reflecting mechanism are too complex to be modeled in a practical way. In this research, only the spectral features are considered for the whitecaps based on Koepke [26]. As for the water-leaving reflectance, the value is usually small compared with the other two components, but it could still bring up to a 10% increase of the OWA in some of the coastal sea areas. Therefore, TCOWA prefers inputting the established remote sensing reflectance product to parameterize the water-leaving component of the OWA, instead of the optical constituents in original three-component models employed by Austin [25], Koepke [26], and Sayer *et al.* [27].

Upon the generation of a global OWA, the ocean color products from MODIS Aqua and the reanalysis data from MERRA provide input for TCOWA, and the output includes clear-sky and white-sky OWAs, both at local noon and in sense of daily mean. The generated examples indicate that the local noon clear-sky OWA shows a significant latitude variation due to the dominant determinant of the solar angle, whereas the white-sky OWA is more sensitive to the wind speed and optical constituents. The global distribution of the daily mean OWA shows a similar trend to the local noon OWA. However, the daily mean clear-sky OWA is significantly larger than the local noon OWA, and this should be noted when using OWA products for energy balance research. In addition, all OWA products exhibit an increase in coastal areas with a high input of terrestrial matter.

It should be mentioned that other data sources could be also employed in the TCOWA. For example, ocean color remote sensing products from Sea-Viewing Wide Field-of-View Sensor (SeaWiFS) or MEdium Resolution Imaging Spectrometer (MERIS) and wind field from reanalysis data of National Centers for Environmental Prediction (NCEP)/National Center for Atmospheric Research (NCAR) could be used. The current input data sources are chosen for their high spatial and temporal resolutions, as well as for their user-friendly access. For the input of ocean color parameters, we will try to combine data from different satellite sensors. However, there is a problem with the temporal resolution of the remote sensing data. The ocean color program releases products at five temporal resolutions, namely, daily, eight-day, monthly, seasonal, and yearly. Among them, the daily product is in demand for instantaneous and daily mean OWA generation, but it suffers from large areas of missing data mainly caused by cloud coverage. Thus, some data fusion and filtering algorithms (e.g., Liu *et al.* [82]) would be applied, as preprocess, to complete the data gaps. For the input of wind field parameters, we still need to cautiously evaluate different reanalysis data sets. Furthermore, we cannot ignore the presence of wind speed products from microwave observations, which are more realistic and have higher spatial resolution.

Another important aspect that this paper does not cover is sea ice and its impact on the global ocean surface albedo. The sea ice makes a large contribution to the reflection of solar radiation

at high latitudes for its high albedo; and the sea ice/albedo feedback mechanism of the climate change has long got the attention of researchers. Although this study chooses to focus on the albedo of ocean water surface and ignores the sea ice, the impact of sea ice albedo has been studied by our colleagues and considered in the new version of GLASS albedo product (e.g., Qu *et al.* [83]); a complete data set of Earth surface albedo, including land, ocean water, and sea ice, is the ultimate goal of our study.

In summary, the TCOWA algorithm could estimate the OWA accurately and generate the global OWA efficiently from remote sensing and meteorological reanalysis data. However, considerable research remains to be done on OWA, either with theoretical studies or with engineering treatments, to meet the needs of climate researchers more effectively.

ACKNOWLEDGMENT

The authors would like to thank all the members in the "Radiation Transfer Research Group" in the Institute of Remote Sensing and Digital Earth (RADI), Chinese Academy of Sciences for their valuable discussions and encouragements. They would also like to thank two anonymous reviewers for their helpful comments.

REFERENCES

[1] T. Dickey and P. Falkowski, "Solar energy and its biological-physical interactions in the sea," in *The Sea*, vol. 12, Biological-Physical Interactions in the Seas. Hoboken, NJ, USA: Wiley, 2002, ch. 10, sec. 2, p. 403.

[2] W. Lucht, C. B. Schaaf, and A. H. Strahler, "An algorithm for the retrieval of albedo from space using semiempirical BRDF models," *IEEE Trans. Geosci. Remote Sens.*, vol. 38, no. 2, pp. 977–998, Mar. 2000.

[3] D. Wang, S. Liang, T. He, and Y. Yu, "Direct estimation of land surface albedo from VIIRS data: Algorithm improvement and preliminary validation," *J. Geophys. Res., Atmos.*, vol. 118, no. 22, pp. 12 577–12 586, Nov. 2013.

[4] S. Liang *et al.*, "A long-term Global Land Surface Satellite (GLASS) data-set for environmental studies," *Int. J. Digit. Earth*, vol. 6, no. 1, pp. 5–33, Dec. 2013.

[5] J.-P. Muller *et al.*, "The ESA globAlbedo project: Algorithm," in *Proc. IEEE IGARSS*, Munich, Germany, Jul. 22–27, 2012, pp. 5745–5748.

[6] A. Riihela, V. Laine, V. Manninen, T. Vihma, and T. Palo, "Surface albedo of the inner Arctic: Validation of the Climate-SAF satellite albedo product with in-situ observations," in *Proc. IEEE IGARSS*, Honolulu, HI, USA, Jul. 25–30, 2010, pp. 1745–1748.

[7] A. Riihelä, T. Manninen, V. Laine, K. Andersson, and F. Kaspar, "CLARA-SAL: A global 28 yr timeseries of Earth's black-sky surface albedo," *Atmos. Chem. Phys.*, vol. 13, no. 7, pp. 3743–3762, Apr. 2013.

[8] F. A.-M. Bender, H. Rodhe, R. J. Charlson, A. M. L. Ekman, and N. Loeb, "22 views of the global albedo—Comparison between 20 GCMs and two satellites," *Tellus*, vol. 58A, no. 3, pp.320–330, May 2006.

[9] S. Wang, A. P. Trishchenko, K. V. Khlopenkov, and A. Davidson, "Comparison of international panel on climate change fourth assessment report climate model simulations of surface albedo with satellite products over northern latitudes," *J. Geophys. Res.*, vol. 11, no. D21, 2006, Art. ID. D21108.

[10] B. P. Briegleb, P. Minnis, V. Ramanathan, and E. Harrison, "Comparison of regional clear-sky albedos inferred from satellite observations and model computations," *J. Clim. Appl. Meteorol.*, vol. 25, no. 2, pp. 214–226, Feb. 1986.

[11] C. Schlick, "Divers éléments pour une synthèse d'images réalistes," Ph.D. dissertation, Univ. Bordeaux 1, Talence, France, 1992.

[12] J. P. Taylor, J. M. Edwards, M. D. Glew, P. Hignett, and A. Slingo, "Studies with a flexible new radiation code—II: Comparisons with aircraft short-wave observations," *Q. J. R. Meteorol. Soc.*, vol. 122, no. 532, pp. 839–861, Apr. 1996.

[13] J. Hansen *et al.*, "Efficient three-dimensional global models for climate studies: Models I and II," *Mon. Weather Rev.*, vol. 111, no. 4, pp. 609–662, Apr. 1983.

[14] C. Cox and W. Munk, "Measurement of the roughness of the sea surface from photographs of the sun's glitter," *J. Opt. Soc. Amer.*, vol. 44, no. 11, pp. 838–850, Nov. 1954.

[15] T. Enomoto, "Ocean surface albedo in AFES," *JAMSTEC Rep. R&D*, vol. 6, pp. 21–30, Nov. 2007.

[16] S. Q. Duntley, "Measurements of the distribution of water wave slopes," *J. Opt. Soc. Amer.*, vol. 44, no. 7, pp. 574–575, Jul. 1954.

[17] C. Cox and W. Munk, "Slopes of the sea surface deduced from photographs of sun glitter," *Bull. Scripps Inst. Oceanogr.*, vol. 6, no. 9, pp. 401–488, Sep. 1956.

[18] J. Wu, "Wind stress and surface roughness at air–sea interface," *J. Geophys. Res.*, vol. 74, no. 2, pp. 444–455, Jan. 1969.

[19] J. I. Gordon, "Directional radiance (luminance) of the sea surface," Visibility Lab., Scripps Inst. Oceanogr., San Diego, CA, USA, SIO Reference 69-20, 1969.

[20] M. S. Longuet-Higgins, "On the skewness of sea-surface slopes," *J. Phys. Oceanogr.*, vol. 12, no. 11, pp. 1283–1291, Nov. 1982.

[21] C. D. Mobley, *Light and Water: Radiative Transfer in Natural Waters*. San Diego, CA, USA: Academic, 1994.

[22] Z. Jin, T. P. Charlock, K. Rutledge, K. Stamnes, and Y. Wang, "Analytical solution of radiative transfer in the coupled atmosphere–ocean system with a rough surface," *Appl. Opt.*, vol. 45, no. 28, pp. 7443–7455, Oct. 2006.

[23] F. Fell and J. Fischer, "Numerical simulation of the light field in the atmosphere–ocean system using the matrix-operator method," *J. Quant. Spectrosc. Radiat. Transf.*, vol. 69, no. 3, pp. 351–388, May 2001.

[24] X. He, Y. Bai, Q. Zhu, and F. Gong, "A vector radiative transfer model of coupled ocean–atmosphere system using matrix-operator method for rough sea-surface," *J. Quant. Spectrosc. Radiat. Transf.*, vol. 111, no. 10, pp. 1426–1448, Jul. 2010.

[25] R. W. Austin, "The remote sensing of spectral radiance from below the ocean surface," in *Optical Aspects of Oceanography*, N. G. Jerlov and E. Steemann-Nielsen, Eds. New York, NY, USA: Academic, 1974, pp. 317–344.

[26] P. Koepke, "Effective reflectance of oceanic whitecaps," *Appl. Opt.*, vol. 23, no. 11, pp. 1816–1824, Jun. 1984.

[27] A. M. Sayer, G. E. Thomas, and R. G. Grainger, "A sea surface reflectance model for (A) ATSR, and application to aerosol retrievals," *Atmos. Meas. Tech.*, vol. 3, no. 4, pp. 813–838, Jul. 2010.

[28] Z. Jin, Y. Qiao, Y. Wang, Y. Fang, and W. Yi, "A new parameterization of spectral and broadband ocean surface albedo," *Opt. Exp.*, vol. 19, no. 27, pp. 26429–26443, Dec. 2011.

[29] C. D. Mobley and E. S. Boss, "Improved irradiances for use in ocean heating, primary production, and photo-oxidation calculations," *Appl. Opt.*, vol. 51, no. 27, pp. 6549–6560, Sep. 2012.

[30] Z. Jin, T. P. Charlock, W. L. Smith, and K. Rutledge, "A parameterization of ocean surface albedo," *Geophys. Res. Lett.*, vol. 31, no. 22, Nov. 2004, Art. ID. L22301.

[31] H. R. Gordon and M. Wang, "Surface-roughness considerations for atmospheric correction of ocean color sensors—I: The Rayleigh-scattering component," *Appl. Opt.*, vol. 31, no. 21, pp. 4247–4260, Jul. 1992.

[32] A. Morel and S. Maritorena, "Bio-optical properties of oceanic waters: A reappraisal," *J. Geophys. Res., Oceans*, vol. 106, no. C4, pp. 7163–7180, Apr. 2001.

[33] A. Morel, D. Antoine, and B. Gentili, "Bidirectional reflectance of oceanic waters: Accounting for Raman emission and varying particle scattering phase function," *Appl. Opt.*, vol. 41, no. 30, pp. 6289–6306, Oct. 2002.

[34] A. Callaghan, G. de Leeuw, L. Cohen, and D. O'Dowd, "Relationship of oceanic whitecap coverage to wind speed and wind history," *Geophys. Res. Lett.*, vol. 35, no. 23, Dec. 2008, Art. ID. L23609.

[35] E. Hecht, *Optics*. 2nd ed. Reading, MA, USA: Addison-Wesley, 1987.

[36] L. Bourg, F. Montagner, V. Billat, and S. Bélanger, "MERIS ATBD 2.13: Sun glint flag algorithm V. 4.3." [Online]. Available: http://envisat.esa.int/instruments/meris/pdf/atbd_2_13.pdf

[37] H. Zhang and M. Wang, "Evaluation of sun glint models using MODIS measurements," *J. Quant. Spectrosc. Radiat. Transf.*, vol. 111, no. 3, pp. 492–506, Feb. 2010.

[38] J. Wu, "Sea-surface slope and equilibrium wind-wave spectra," *Phys. Fluids*, vol. 15, no. 5, pp. 741–747, May 1972.

[39] M. D. Mermelstein, E. P. Shettle, E. H. Takken, and R. G. Priest, "Infrared radiance and solar glint at the ocean-sky horizon," *Appl. Opt.*, vol. 33, no. 25, pp. 6022–6034, Sep. 1994.

[40] J. A. Shaw and J. H. Churnside, "Scanning-laser glint measurements of sea-surface slope statistics," *Appl. Opt.*, vol. 36, no. 18, pp. 4202–4213, Jun. 1997.

[41] N. Ebuchi and S. Kizu, "Probability distribution of surface wave slope derived using sun glitter images from geostationary meteorological satellite and surface vector winds from scatterometers," *J. Oceanogr.*, vol. 58, no. 3, pp 477–486, Jun. 2002.
[42] P. M. Saunders, "Shadowing on the ocean and the existence of the horizon," *J. Geophys. Res.*, vol. 72, no. 18, pp. 4643–4649, Sep. 1967.
[43] M. D. Anguelova and F. Webster, "Whitecap coverage from satellite measurements: A first step toward modeling the variability of oceanic whitecaps," *J. Geophys. Res., Oceans*, vol. 111, no. C3, Mar. 2006, Art. ID. C03017.
[44] E. C. Monahan, "Whitecaps and foam," in *Encyclopedia of Ocean Sciences*, vol. 6. New York, NY, USA: Academic, 2001, pp. 3213–3219.
[45] R. E. Payne, "Albedo of the sea surface," *J. Atmos. Sci.*, vol. 29, no. 5, pp. 959–970, Jul. 1972.
[46] C. H. Whitlock, D. S. Bartlett, and E. A. Gurganus, "Sea foam reflectance and influence on optimum wavelength for remote sensing of ocean aerosols," *Geophys. Res. Lett.*, vol. 9, no. 6, pp. 719–722, Jun. 1982.
[47] R. Frouin, M. Schwindling, and P-Y. Deschamps, "Spectral reflectance of sea foam in the visible and near-infrared: In situ measurements and remote sensing implications," *J. Geophys. Res.*, vol. 101, no. C6, pp. 14 361–14 371, Jun. 1996.
[48] K. D. Moore, K. J. Voss, and H. R. Gordon, "Spectral reflectance of whitecaps: Their contribution to water-leaving radiance," *J. Geophys. Res., Oceans*, vol. 105, no. C3, pp. 6493–6499, Mar. 2000.
[49] J.-M. Nicolas, P.-Y. Deschamps, and R. Frouin, "Spectral reflectance of oceanic whitecaps in the visible and near infrared: Aircraft measurements over open ocean," *Geophys. Res. Lett.*, vol. 28, no. 23, pp. 4445–4448, Dec. 2001.
[50] A. A. Kokhanovsky, "Spectral reflectance of whitecaps," *J. Geophys. Res., Oceans*, vol. 109, no. C5, May 2004, Art. ID. C05021.
[51] E. C. Monahan, "Oceanic whitecaps," *J. Phys. Oceanogr.*, vol. 1, no. 2, pp. 139–144, Mar. 1971.
[52] E. C. Monahan and I. G. O'Muircheartaigh, "Whitecaps and the passive remote sensing of the ocean surface," *Int. J. Remote Sens.*, vol. 7, no. 5, pp. 627–642, May 1986.
[53] E. C. Monahan and I. G. O'Muircheartaigh, "Optimal power-law description of oceanic whitecap coverage dependence on wind speed," *J. Phys. Oceanogr.*, vol. 10, no. 12, pp. 2094–2099, Dec. 1980.
[54] A. Ignatov and L. Stowe, "Aerosol retrievals from individual AVHRR channels—Part I: Retrieval algorithm and transition from Dave to 6S radiative transfer model," *J. Atmos. Sci*, vol. 59, no. 3, pp. 313–334, Feb. 2002.
[55] C. D. Mobley, H. Zhang, and K. J. Voss, "Effects of optically shallow bottoms on upwelling radiances: Bidirectional reflectance distribution function effects," *Limnol. Oceanogr.*, vol. 48, no. 1, pp. 337–345, Jan. 2003.
[56] H. R. Gordon *et al.*, "A semianalytic radiance model of ocean color," *J. Geophys. Res., Atmos.*, vol. 93, no. D9, pp. 10 909–10 924, Sep. 1988.
[57] A. Morel, "Optical modeling of the upper ocean in relation to its biogenous matter content (case I waters)," *J. Geophys. Res., Oceans*, vol. 93, no. C9, pp. 10 749–10 768, Sep. 1988.
[58] A. Morel and B. Gentili, "Diffuse reflectance of oceanic waters: Its dependence on sun angle as influenced by the molecular scattering contribution," *Appl. Opt.*, vol. 30, no. 30, pp. 4427–4438, Oct. 1991.
[59] A. Morel and B. Gentili, "Diffuse reflectance of oceanic waters—II: Bidirectional aspects," *Appl. Opt.*, vol. 32, no. 33, pp. 6864–6879, Nov. 1993.
[60] A. Morel and B. Gentili, "Diffuse reflectance of oceanic waters—III: Implication of bidirectionality for the remote-sensing problem," *Appl. Opt.*, vol. 35, no. 24, pp. 4850–4862, Aug. 1996.
[61] C. D. Mobley, D. Stramski, W. P. Bissett, and E. Boss, "Optical modeling of ocean waters: Is the case 1-case 2 classification still useful?" *Oceanography*, vol. 17, no. 2, pp. 60–67, Jun. 2004.
[62] Z. P. Lee and C. M. Hu, "Global distribution of Case-1 waters: An analysis from SeaWiFS measurements," *Remote Sens. Environ.*, vol. 101, no. 2, pp. 270–276, Mar. 2006.
[63] E. Boss, W. S. Pegau, J. R. V. Zaneveld, and A. H. Barnard, "Spatial and temporal variability of absorption by dissolved material at a continental shelf," *J. Geophys. Res., Oceans*, vol. 106, no. C5, pp. 9499–9507, May 2001.
[64] M. Babin *et al.*, "Variations in the light absorption coefficients of phytoplankton, nonalgal particles, and dissolved organic matter in coastal waters around Europe," *J. Geophys. Res.*, vol. 108, no. C7, p. 3211, Jul. 2003.
[65] M. Babin *et al.*, "Light scattering properties of marine particles in coastal and open ocean waters as related to the particle mass concentration," *Limnol. Oceanogr.*, vol. 48, no. 2, pp. 843–859, Mar. 2003.
[66] D. G. Bowers and C. E. Binding, "The optical properties of mineral suspended particles: A review and synthesis," *Estuarine Coastal Shelf Sci.*, vol. 67, no. 1/2, pp. 219–230, Mar. 2006.
[67] B. A. Franz, Algorithm for Retrieval of Remote Sensing Reflectance from Satellite Ocean Color Sensors, Mar. 20, 2015. [Online]. Available: http://oceancolor.gsfc.nasa.gov/WIKI/AtmoCor.html
[68] R. P. Bukata, J. H. Jerome, A. S. Kondratyev, and D. V. Pozdnyakov, *Optical Properties and Remote Sensing of Inland and Coastal Waters*. Boca Raton, FL, USA: CRC Press, 1995.
[69] G. Schaepman-Strub, M. E. Schaepman, T. H. Painter, S. Dangel, and J. V. Martonchik, "Reflectance quantities in optical remote sensing—Definitions and case studies," *Remote Sens. Environ.*, vol. 103, no. 1, pp. 27–42, Jul. 2006.
[70] A. Morel, K. J. Voss, and B. Gentili, "Bidirectional reflectance of oceanic waters: A comparison of modeled and measured upward radiance fields," *J. Geophys. Res.*, vol. 100, no. C7, pp. 13 143–13 151, Jul. 2006.
[71] C. D. Mobley *et al.*, Ocean Optics WebBook, Jan. 3, 2014. [Online]. Available: http://www.oceanopticsbook.info/view/radiative_transfer_theory/level_2/measures_of_reflectance
[72] J. Ronald and V. Zaneveld, "A theoretical derivation of the dependence of the remotely sensed reflectance of the ocean on the inherent optical properties," *J. Geophys. Res.*, vol. 100, no. C7, pp. 13 135–13 142, Jul. 1991.
[73] Z. P. Lee *et al.*, "An inherent-optical-property-centered approach to correct the angular effects in water-leaving radiance," *Appl. Opt*, vol. 50, no. 19, pp. 3155–3167, Jul. 2011.
[74] C. N. Long and T. P. Ackerman, "Identification of clear skies from broadband pyranometer measurements and calculation of downwelling shortwave cloud effects," *J. Geophys. Res.*, vol. 105, no. D12, pp. 15 609–15 626, Jun. 2000.
[75] G. M. Hale and M. R. Querry, "Optical constants of water in the 200 nm to 200 μm wavelength region," *Appl. Opt.*, vol. 12, no. 3, pp. 555–563, Mar. 1973.
[76] S. Liang, "Narrowband to broadband conversions of land surface albedo—I: Algorithms," *Remote Sens. Environ.*, vol. 76, no. 2, pp. 213–238, May 2001.
[77] M. I. Sancer, "Shadow-corrected electromagnetic scattering from a randomly rough surface," *IEEE Trans. Antennas Propag.*, vol. AP-17, no. 5, pp. 577–585, Sep. 1969.
[78] Z. Jin, T. P. Charlock, and K. Rutledge, "Analysis of broadband solar radiation and albedo over the ocean surface at COVE," *J. Atmos. Ocean. Technol.*, vol. 19, no. 10, pp. 1585–1601, Oct. 2002.
[79] T. Manninen, A. Riihelä, and G. de Leeuw, "Atmospheric effect on the ground-based measurements of broadband surface albedo," *Atmos. Meas. Tech.*, vol. 5, no. 1, pp. 385–409, Jan. 2012.
[80] R. W. Gould, Jr., R. A. Arnone, and P. M. Martinolich, "Spectral dependence of the scattering coefficient in case 1 and case 2 waters," *Appl. Opt.*, vol. 38, no. 12, pp. 2377–2383, Apr. 1999.
[81] Z. Li and L. Garand, "Estimation of surface albedo from space: A parameterization for global application," *J. Geophys. Res., Atmos.*, vol. 99, no. D4, pp. 8335–8350, Apr. 1994.
[82] N. Liu, Q. Liu, L. Wang, and J. Wen, "A temporal filtering algorithm to reconstruct daily albedo series based on GLASS albedo product," in *Proc. IEEE IGARSS*, Vancouver, BC, Canada, Jul. 24–29, 2011, pp. 4277–4288.
[83] Y. Qu, Q. Liu, Y. Feng, S. Liu, and S. Liang, "Estimating Arctic sea-ice shortwave albedo from MODIS data," *Remote Sens. Environ*, to be published.

Youbin Feng was born in Funan County, Anhui Province, China, in 1989. He received the B.S. degree in marine sciences from the Dalian Maritime University, Dalian, China, in 2006 and the M.S. degree in global environment change (major in quantitative remote sensing) from Beijing Normal University, Beijing, China, in 2014.

He is currently with the State Key Laboratory of Remote Sensing Science, College of Global Change and Earth System Science, Beijing Normal University. His research interests include the radiative transfer through the atmosphere–water interface and the data analysis approach.

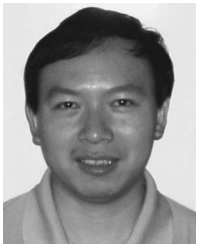

Qiang Liu was born in Kunming City, Yunnan Province, China, in 1974. He received the B.S. degree in computational mathematics from Beijing University, Beijing, China, in 1997 and the Ph.D. degree in cartography and remote sensing from the Institute of Remote Sensing Applications, Chinese Academy of Sciences, Beijing, in 2002.

He is currently an Associate Professor with the College of Global Change and Earth System Science, Beijing Normal University and also with the State Key Laboratory of Remote Sensing Science, jointly sponsored by Beijing Normal University and the Institute of Remote Sensing and Digital Earth, Chinese Academy of Sciences. His research interests are about multiangular remote sensing, including geometric processing of multiangular images, BRDF/albedo modeling, and component temperature retrieval. His current research is to generate long time series of global BRDF/albedo from multiple remote sensing data sources.

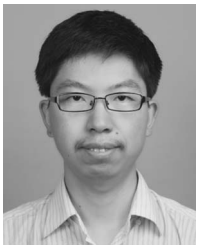

Ying Qu received the B.S. and Ph.D. degrees in geographical information science from Beijing Normal University, Beijing, China, in 2008 and 2013, respectively.

From 2013 to 2015, he was a Postdoctoral Researcher with Beijing Normal University. Since 2015, he has been an Associate Professor with the School of Geographical Sciences, Northeast Normal University, Changchun, China. His research interests focus on monitoring the global environmental and climatic changes from satellite observations.

Shunlin Liang (M'94–F'13) received the Ph.D. degree from Boston University, Boston, MA, USA, in 1993.

He is currently a Professor with the Department of Geographical Sciences, University of Maryland, College Park, MD, USA, and the School of Geography, Beijing Normal University, Beijing, China. He has authored or coauthored over 220 SCI indexed journal papers, authored the book *Quantitative Remote Sensing of Land Surfaces* (Wiley, 2004), coauthored the book *Global LAnd Surface Satellite (GLASS) Products: Algorithms, Validation and Analysis* (Springer, 2013), edited the book *Advances in Land Remote Sensing: System, Modeling, Inversion and Application* (Springer, 2008), and coedited the books *Advanced Remote Sensing: Terrestrial Information Extraction and Applications* (Academic Press, 2012) and *Land Surface Observation, Modeling, Data Assimilation* (World Scientific, 2013). His main research interests focus on estimation of land surface variables from satellite data, earth energy balance, and assessment of environmental changes.

Prof. Liang has served an Associate Editor of the IEEE TRANSACTIONS ON GEOSCIENCE AND REMOTE SENSING and a Guest Editor of several remote-sensing-related journals.